Title
Snow-eater heat waves of the western United States

Journal
Science Advances, 12(32)

ISSN
2375-2548

Authors
Rhoades, Alan M

North, Joshua Snowball

Rudisill, William

et al.

Publication Date
2026-08-07

DOI
10.1126/sciadv.aeb3361

ATMOSPHERIC SCIENCE

Snow-eater heat waves of the western United States

Alan M. Rhoades[1]*, Joshua Snowball North[1], William Rudisill[1], Benjamin J. Hatchett[2], Mark Risser[1], Areidy Beltran-Peña[3], Anne Heggli[4], Scott Hotaling[5], Laurie S. Huning[6], Andrew Joros[4], Matthew LaPlante[5], Ankur Mahesh[1,7], Adrienne M. Marshall[8], Rachel McCrary[9], Daniel McEvoy[4], Stefan Rahimi[10], Mark S. Raleigh[11], Calen Randall[12], Abhishekh Srivastava[12], Michael Wehner[1], Yang Zhou[1], Andrew D. Jones[1,7]

Abrupt snowmelt, triggered by rain-on-snow events or "snow-eater heat waves," can cause flooding, initiate or accelerate snow drought, and affect water availability. However, the characteristics (e.g., area, duration, and frequency), impacts, and trends of snow-eater heat waves have received little attention. To address this gap, we developed a method to identify snow-eater heat waves and estimate their melt potential using 20th Century Reanalysis version 3 air temperature data, the TempestExtremes algorithm, and an operational snowmelt model (SNOW-17) across 1850–2015. Melt season snow-eater heat waves typically last 3 to 5 days, with three to five events, doubling snowmelt rates. Seven of 11 spring superfloods are shown to coincide with snow-eater heat waves. Since the 1850s, snow-eater heat waves have increased in area and frequency, decreased in duration, and shifted earlier in the melt season. Incorporating snow-eater heat-wave impacts into SNOW-17 enhances extreme melt estimates, improving water management support tools.

INTRODUCTION

In the western United States (WUS), heat waves occur regularly in the spring and early summer and have nearly doubled in frequency and intensity since the mid-1990s (*1*). It is "virtually certain" that climate change has driven the shift in heat-wave timing, intensity, and frequency (*2*). Spring and early summer heat waves can rapidly diminish snowpacks, a phenomenon we term here as "snow-eater heat waves." We qualitatively define snow-eater heat waves as seasonally anomalous and consistent above-freezing temperature conditions that are sustained (i.e., day and night) for several days, resulting in impacts to water resources (e.g., warm-season water supply allocations) and increases in flood hazard. By developing observational and model-based quantitative criteria producing snow-eater heat-wave events (see Materials and Methods), we find that these events are distinct from warm spells and conventional heat waves (Fig. 1).

In recent decades, snow-eater heat waves have occurred several times in the WUS, often following the buildup of a snowpack in the month(s) before the ablation event. For example, in 1983, a spring "superflood" struck northern Utah, where rapid snowmelt overtook low-lying communities between the Wasatch Mountains and the Great Salt Lake (*3*). Given the hydrological importance of this event, we treat it here as a case study of snow-eater heat waves. As described by Arnow (*4*), "...major snowmelt began at the end of May, during a heat wave on the Memorial Day weekend; and record-breaking quantities of water flowed into the lake from many tributary streams..." Nine streams on the Wasatch Front reached flood stage, and Salt Lake City was forced to construct two emergency canals (*5*). That same week, extreme snowmelt, following a near-record snowpack season, triggered a fatal landslide in western Nevada (*6*). Later, rapid snowmelt-driven rises in Lake Powell water levels from June until July (180% of normal) necessitated emergency measures to protect Glen Canyon Dam from overtopping and continued cavitation of the spillway (*7*).

In 2021, a series of events occurred in the WUS and appeared to share the characteristics of snow-eater heat waves. During early April, mean air temperature anomalies exceeded +4 to 8 K, with associated widespread declines in snowpack: 24% of measurement sites reported median snow water equivalent (SWE) changes of at least −99 mm, or −14 mm/day, with particularly anomalous conditions occurring in the coastal WUS (*8*). Between June 26 and 29, the Pacific Northwest experienced another period of anomalous heat and rapid snowmelt, shattering temperature records throughout the Pacific Northwest by up to 5 K (*9*). The snow-covered areas of the Pacific Northwest were 35% above normal on 1 April but fell from 31 to 12% of normal between 25 and 30 June (*1*).

Research on the impact of heat waves and warm spells during the winter and spring seasons on snowpack is limited. Previous studies have primarily focused on near-term historical records or served as regional attribution analyses using more conventional heat-wave event criteria, such as the exceedance of a certain percentile of daily maximum temperature (e.g., 90th or 99th percentile) or above a fixed temperature threshold for a given number of days (e.g., 3 days) (*1*, *8*, *10*–*18*). Except for Scaff *et al.* (*17*) and Deng *et al.* (*18*), many of the criteria do not necessarily account for snowpack energy budget–specific requirements, such as sustained above-freezing temperatures through the day and night that erode cold content and/or drive snowmelt. Thus, snow-eater heat-wave events represent an important knowledge gap in the literature.

Snow-eater heat-wave events are distinct from other drivers of snowmelt extremes, such as rain-on-snow events and warm spells (Fig. 1). Unlike rain-on-snow events, which are shaped by low-pressure troughs that promote the inland penetration of warm and moist air (*3*, *19*–*23*), snow-eater heat waves result from alternative synoptic-to-mesoscale mechanisms that we explore in this study (e.g., amplified, stationary high-pressure ridges). Distinct from warm spells

[1]Lawrence Berkeley National Laboratory, Berkeley, CA, USA. [2]Colorado State University, Fort Collins, CO, USA. [3]Stanford University, Stanford, CA, USA. [4]Desert Research Institute, Reno, NV, USA. [5]Utah State University, Logan, UT, USA. [6]California State University, Long Beach, CA, USA. [7]University of California, Berkeley, Berkeley, CA, USA. [8]Colorado School of Mines, Golden, CO, USA. [9]National Center for Atmospheric Research, Boulder, CO, USA. [10]University of Wyoming, Laramie, WY, USA. [11]Oregon State University, Corvallis, OR, USA. [12]University of California, Davis, Davis, CA, USA.
*Corresponding author. Email: arhoades@lbl.gov

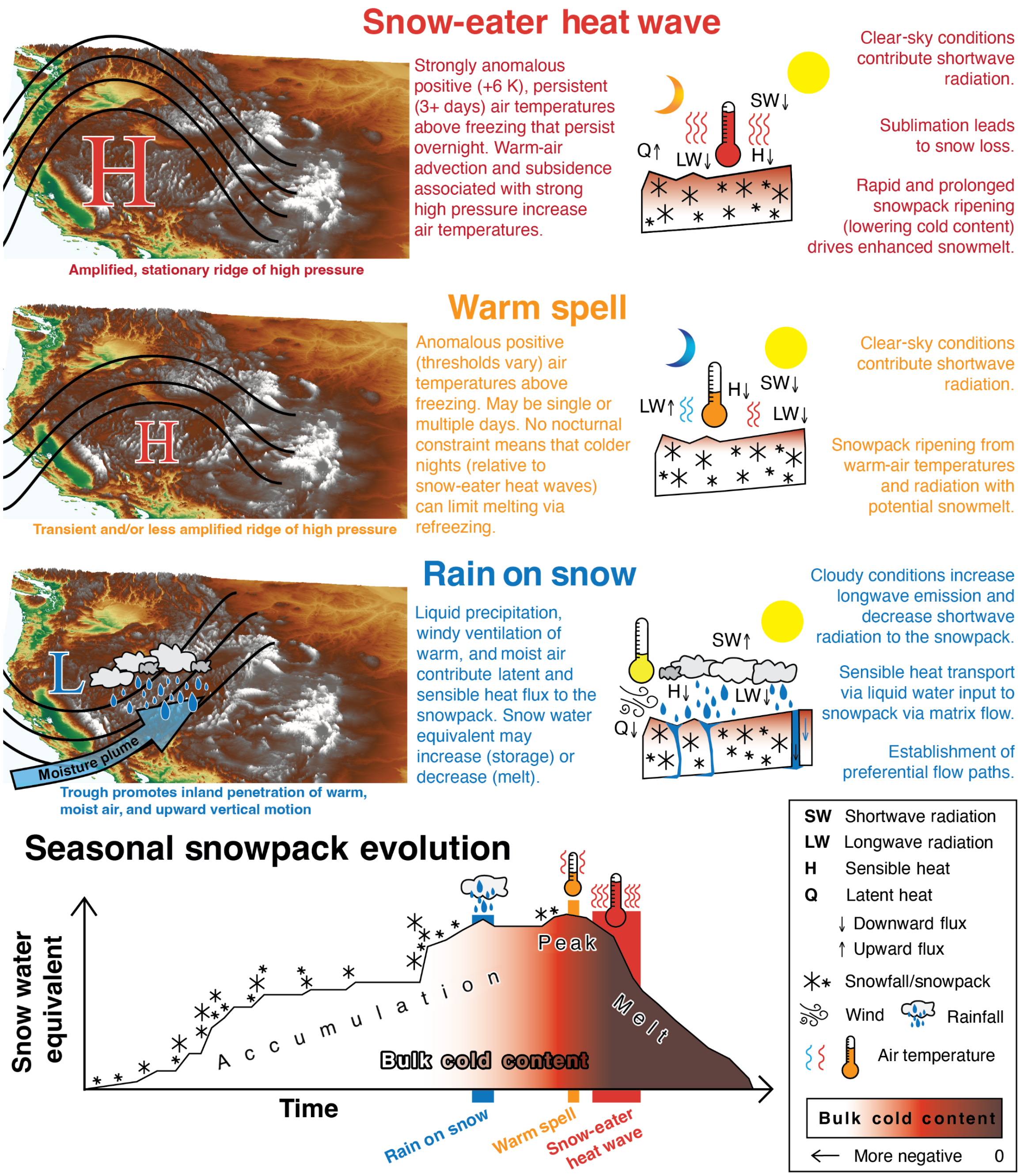

Fig. 1. Snow-process differences between snow-eater heat waves, warm spells, and rain-on-snow events. A schematic that contrasts the differences between WUS snow-eater heat-wave events, warm spells, and rain-on-snow events. These phenomena differ in their synoptic-to-mesoscale atmospheric circulation patterns and surface energy budgets operating at synoptic to microscales (i.e., slope and plot scales) that drive snowpack mass and energy budgets (i.e., cold content). There are also important differences in the timing and persistence of their occurrence in the water year that influence melt potential.

(*11*, *17*), which potentially have more transient and less amplified high-pressure ridges that yield less anomalous heating [i.e., 90th percentile air temperature (*17*)], snow-eater heat-wave events could exhibit more persistence in their air temperature anomalies (over both day and night) that promote more snowpack ripening and enhanced ablation through melt and sublimation. Last, in contrast to more traditional heat-wave metrics [e.g., 3 days of sustained 98th percentile air temperature (*24*)], snow-eater heat-wave temperature criteria should be attuned to snow-related impacts (i.e., above-freezing conditions that persist through the night, allowing melt to continue or that minimize refreezing). The air temperature conditions needed to identify snow-eater heat-wave events and snowpack changes during and after them are explored in this study through site-level to synoptic-scale analyses.

Snow-eater heat waves have been less studied than other snowmelt extremes yet have the potential to increase in area, duration, frequency, and/or intensity in a rapidly changing climate. This is especially likely through the middle of the 21st century, when models suggest that WUS snowpack volumes will increasingly shift toward a "low-to-no snow" future under continued climate warming (*25*). Even in years in which snowpacks remain within historical patterns of variability, middle 21st century snowpacks are likely to be more susceptible to ablation (*14*, *26*). Abrupt spring and early summer snowmelt events can be particularly impactful on WUS water management as these events occur during a time of year when water rights allocations are made (*27*), often with fixed operating rules (*28*), that can exacerbate water gaps in the warm season (*29*). Compoundingly, recent studies indicate that operational forecasts of reservoir inflows systematically underrepresent actual reservoir inflows (particularly in the WUS in recent decades) owing to changes in precipitation and temperature patterns that shape snowmelt-contributed runoff (*30*, *31*). Longer-term predictions of WUS snowpack behavior also show that a deleterious, widespread, and persistent decrease in snowfall and snowpack storage is expected as the WUS continues to warm (*25*, *32*–*34*). These reductions will continue to alter historically assumed snowmelt-contributed runoff and overall runoff efficiency (*26*).

All of these factors may be aggravated by shifts in snow-eater heat-wave area, frequency, duration, and/or intensity, and it is thus important to understand how snow-eater heat-wave characteristics may have changed from historical patterns of variability or may be changing under anthropogenic climate change. This understanding cannot be achieved; however, until snow-eater heat waves are quantitatively defined and characterized. A major question remains as to whether these shifts in snowmelt characteristics occur gradually and/or in a punctuated fashion, shaped by snowmelt extremes such as snow-eater heat waves.

Here, we address the following questions, with a particular focus on the WUS:

1) What criteria for environmental state variables could be used to define snow-eater heat-wave events?

2) Does an operational melt potential model well represent snow-eater heat wave contributed melt potential, or are enhancements needed?

3) What fraction of late spring and early summer melt potential do the largest snow-eater heat-wave events in the historical record contribute?

4) Have snow-eater heat-wave characteristics (i.e., areal extent, intensity, duration, and frequency) changed from the 19th to the early 21st century?

RESULTS

In the following subsections, we will introduce storyline-based (*35*) and climatological-based analyses of WUS snow-eater heat-wave events, the melt potential of which are estimated through a combination of National Oceanic and Atmospheric Administration (NOAA)–Cooperative Institute for Research in Environmental Sciences–US Department of Energy 20th Century Reanalysis version 3 (20CRv3) (*36*–*38*) estimates of 2-m air temperature (T2m) and the National Weather Service's operational snow accumulation and ablation model (SNOW-17) (*39*). A 50-member ensemble of melt potential estimates is generated through the use of a data-informed Bayesian statistical model that identifies optimal SNOW-17 parameter settings across the WUS (see Materials and Methods for more details). Note that melt potential is not actual snowmelt. Rather, it is the maximum amount of melt that could occur if sufficient SWE existed. For the storyline event, we use the snow-eater heat-wave event of 27 to 31 May 1983 to examine the fidelity of the 20CRv3–SNOW-17 melt potential models across all days and snow-eater heat wave–only days between 19 March and 1 July. This storyline event is chosen as it was the top spring season, snowmelt-dominated superflood event between 1950 and 2010 (*3*). We then climatologically contextualize this event across both the Snow Telemetry (SNOTEL) Network (https://nwcc-apps.sc.egov.usda.gov/imap/) period of record (1980–2015) and the longer period of record enabled by 20CRv3 (1850–2015). This process allows us to build a catalog of snow-eater heat-wave events and provide estimates of how their characteristics have changed between the 19th and 21st centuries.

The 1983 snow-eater heat-wave event

Figure 2 compares SNOTEL Network measurements of daily change in SWE (dSWE) with 20CRv3–SNOW-17 melt potential estimates for the May 1983 superflood event across three melt potential models, including the "out-of-the-box" SNOW-17 model, which has no heat-wave hour (NHH) influence, and two experimental models, heat-wave hours (HHs) and accumulative heat-wave hours (AHH). More details about these melt potential models are provided in Materials and Methods. Comparisons between melt potential estimates and observed dSWE measurements are only made with those SNOTEL sites that fall within the snow-eater heat-wave area and up to the point at which SNOTEL SWE reaches 0 mm. We first aggregate across the 50-member ensemble estimates and across SNOTEL stations (or nearest grid cells to the SNOTEL stations) and then estimate the averages and deciles. Between 19 March to 1 July, SNOTEL site daily mean and 90th percentile dSWE were −10.3 and −33.0 mm/day, respectively. On snow-eater heat wave–only days, the mean dSWE was −37.0 mm/day, with a 90th percentile value of −66.0 mm/day. This more than 300% change in dSWE on snow-eater heat wave–only days was also captured by each of the 20CRv3–SNOW-17 model melt potential estimates. The NHH model had a slightly lower mean daily melt potential of −11.4 mm/day, with HH and AHH at −11.6 mm/day.

More divergence between the 20CRv3–SNOW-17 models occurred on snow-eater heat wave–only days due to the experimental model's newly implemented natural log additive melt term (eq. S1). The closest mean estimates of daily melt potential were produced by NHH (−36.6 mm/day), followed by HH (−52.3 mm/day) and AHH (−54.3 mm/day). Although NHH had the best mean daily melt potential performance compared to SNOTEL measurements overall, it failed to capture relatively extreme melt potentials: 90th percentile modeled (−44.8 mm/day) melt potential estimates were more tightly constrained than observations (−66.0 mm/day). Contrastingly, HH (−60.0 mm/day) nearly reached daily melt potentials comparable to the 90th percentile dSWE threshold measured at SNOTEL sites, and AHH (−67.6 mm/day) slightly exceeded the threshold. Across SNOTEL stations, the 1983 snow-eater heat-wave event coincided with a minimal amount of precipitation (fig. S2) and a persistent atmospheric ridge across the WUS (fig. S3).

Snow-eater heat-wave climatology over the SNOTEL period of record

The three 20CRv3–SNOW-17 melt potential models are now compared over climatological timescales, spanning the SNOTEL period of record (1980–2015) that overlaps with 20CRv3 (Fig. 3). WUS-wide

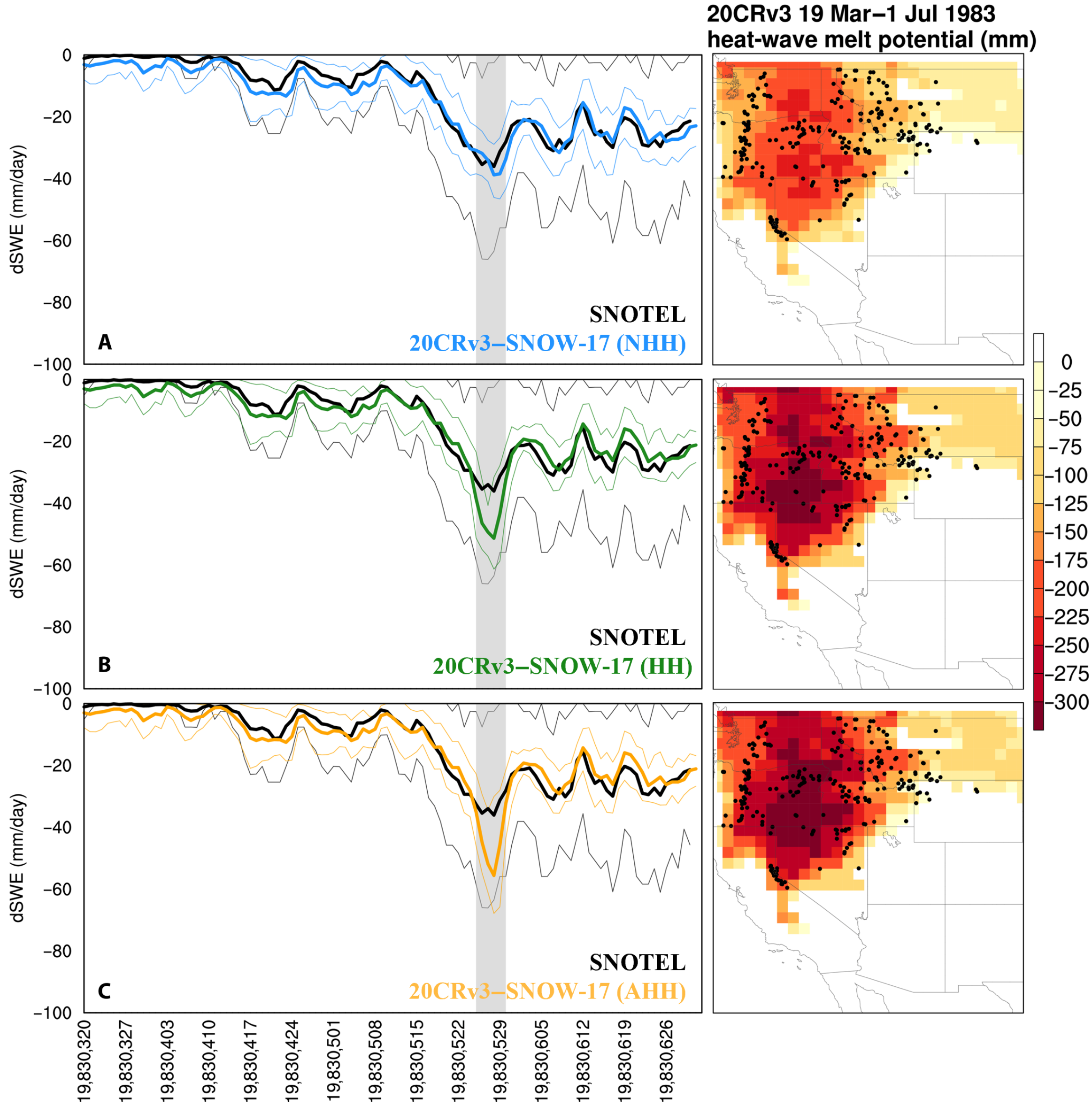

Fig. 2. Year 1983 snow-eater heat-wave event comparison of observed snowmelt and modeled melt potential. Time series comparisons of 20CRv3–SNOW-17 (colored) melt potential with SNOTEL (black) dSWE for 19 March to 1 July 1983. (**A**) The out-of-the-box version of SNOW-17, or the NHH effect, melt potential model. (**B** and **C**) The experimental HH and AHH effect SNOW-17 melt potential models, respectively. The bold lines are 50 ensemble member mean estimates, and the thin lines are the deciles across all sites/nearest grid cells. The gray-shaded region represents the timing and duration of the snow-eater heat-wave event. The map plots show the SNOTEL sites (black dots) used for the comparison (those that fall within the snow-eater heat-wave region) and the heat-wave day accumulative melt potential estimates (in millimeters) by the 20CRv3–SNOW-17 models between 19 March and 1 July.

SNOTEL dSWE, on average, was −9.0 mm/day with the 90th percentile melt at −28.0 mm/day on all days between 19 March and 1 July (Table 1). Each melt potential model overestimated mean daily melt potential compared with SNOTEL by several millimeters per day, with NHH most closely matching SNOTEL (−11.4 mm/day). Climatological decile melt potential on all days was underrepresented by all 20CRv3–SNOW-17 melt potential models. However, NHH was more constrained (−24.4 mm/day) than either HH (−25.9 mm/day) or AHH (−25.7 mm/day). On snow-eater heat wave–only days, SNOTEL dSWE was −16.9 mm/day with the 90th and 99th percentile melt at −35.6 and −61.0 mm/day, respectively. Comparable to the all-day results, NHH best represents mean melt potential on snow-eater heat wave–only days (−22.0 mm/day) but was more constrained on 90th percentile melt (−33.6 mm/day) and, especially, on 99th percentile melt potential (−43.3 mm/day). HH and AHH both overestimate mean melt potentials (−37.8 and −39.6 mm/day) and 90th percentile melt potentials (−50.2 and −56.2 mm/day) on snow-eater heat wave–only days, respectively. Only HH and AHH reach SNOTEL-like 99th percentile melt potentials (−64.4 and −67.2 mm/day, respectively).

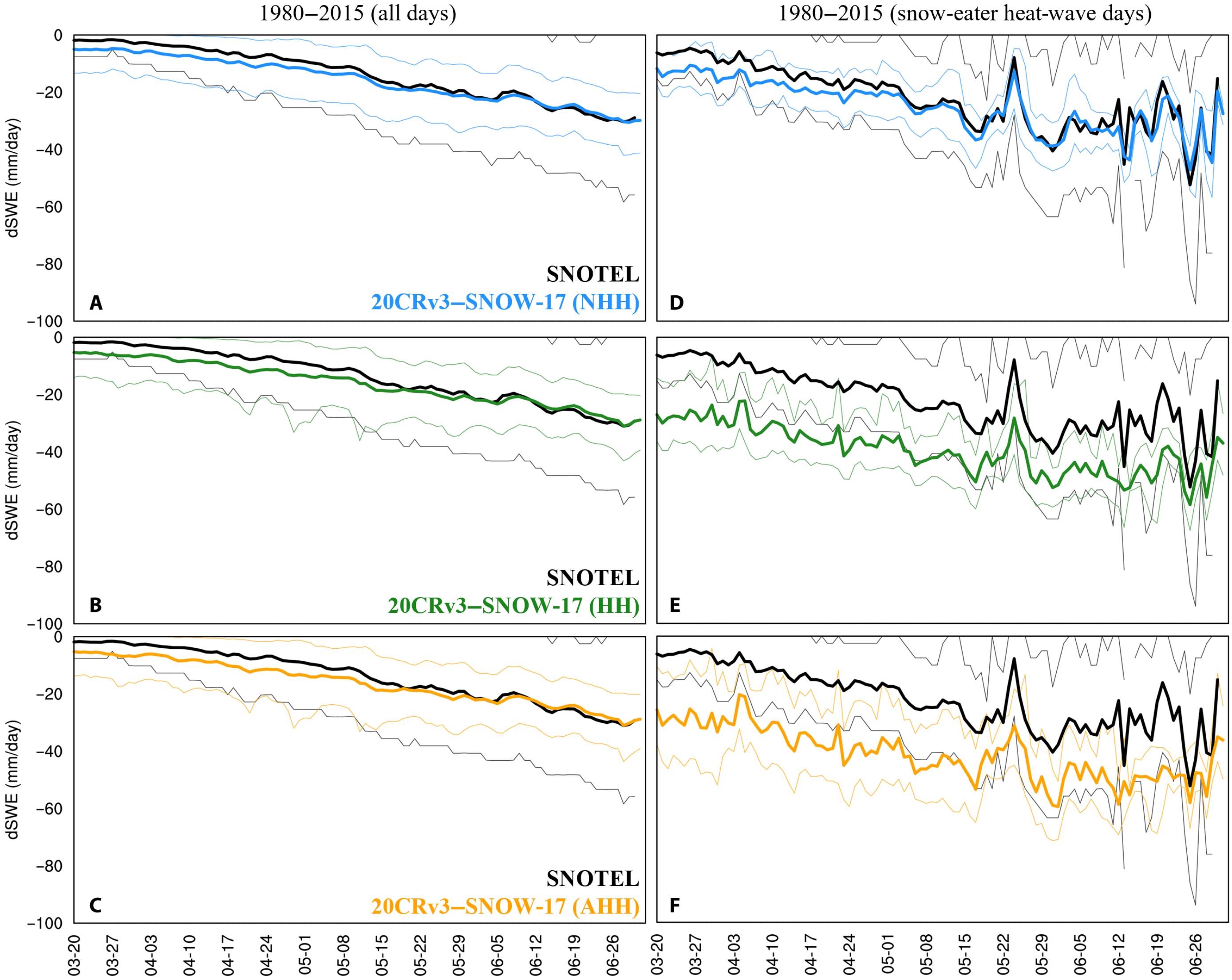

Fig. 3. Climatological (1980–2015) observed snowmelt and modeled melt potential on all days and snow-eater heat wave–only days. Time series comparisons of the daily climatological (1980–2015) average 20CRv3–SNOW-17 (colored) melt potential with SNOTEL (black) dSWE between 19 March and 1 July. Dates are given in MM-DD on the *x* axis. (**A** to **C**) All days between 19 March and 1 July, with (A) being the out-of-the-box version of SNOW-17 or the NHH effect, and (B) and (C) are the experimental HH and AHH effect SNOW-17 models, respectively. (**D** to **F**) Snow-eater heat wave–only days between 19 March and 1 July. Bold lines are 50 ensemble member mean estimates, and the thinner lines are the deciles across all sites/nearest grid cells.

Table 1. Climatological (1980–2015) observed snowmelt summary statistics on all days and snow-eater heat wave–only days. Climatological (1980–2015) summary statistics for the dSWE (in millimeters per day) across WUS SNOTEL stations on all days between 19 March and 1 July and on snow-eater heat wave–only days. Positive dSWE values were set to 0 mm, and missing values were excluded to avoid bias in comparison to the SNOW-17 melt potential estimates (which can not provide positive values). A total of 1,128,750 and 55,523 dSWE measurements were recorded across all stations and years, respectively, for all days and snow-eater heat wave–only days.

Metric (1980–2015)	All days	Snow-eater heatwave days
Mean	−9.0	−17
SD	13	15
Median	−2.0	−15
75th percentile	−15	−25
90th percentile	−28	−36
99th percentile	−53	−61

Figure S4 shows the precipitation rates across WUS SNOTEL stations between 1980 and 2015 that coincide with snow-eater heat-wave events and SWE greater than 0 mm. The number of precipitation station days that co-occurred with snow-eater heat waves and SWE greater than 0 mm was 3121 (∼26% of snow-eater heat-wave station days). Year 1989 accounted for ∼52% of those precipitation station days that co-occur with snow-eater heat waves and SWE greater than 0 mm. Five years (1989, 2015, 2012, 1986, and 2004, in order of percent contribution) accounted for ∼78% of the precipitation station days. In addition, if you remove all station days within the top 5 years of snow-eater heat wave and rain-on-snow co-occurrence, SNOTEL −dSWE rates are enhanced (−2 to −3 mm/day) (table S1). Therefore, we find it less likely that rain-on-snow and snow-eater heat-wave events co-occur and, when they co-occur, melt rates are lower than during snow-eater heat wave–only events. This is likely due to the presence of amplified and persistent high-pressure ridges during snow-eater heat waves (fig. S5). These features block atmospheric rivers associated with midlatitude cyclones from making landfall, which can bring heavy rainfall to high elevations during spring (*40*).

To contextualize the severity of the 1983 snow-eater heat-wave event relative to all 5-day maximum daily melt potential events (Mx5day), we now compare 1983 to all Mx5day events within the SNOTEL period of record (table S2). Notably, all values presented are melt potential, not actual snowmelt. The 1983 snow-eater heat-wave event Mx5day ranked numbers 13 to 16 (based on the use of NHH, HH, or AHH). The top five Mx5day events in the SNOTEL period of record occurred in 2014 (84.1 km^3), 2015 (76.7 km^3), 1992 (72.9 km^3), 1986 (72.2 km^3), and 2013 (58.7 km^3).

We now compare total snow-eater heat-wave melt potential estimated for 1983 with all seasons between 1980 and 2015 using the 20CRv3–SNOW-17 NHH model over the SNOTEL period of record that overlaps with 20CRv3 (1980–2015; table S3). The year with the highest mean seasonal total melt potential contributed by snow-eater heat waves during the period between 1980 and 2015 occurred in 2015 at 152 km^3 or 23% of the total melt potential of 652 km^3 between 19 March and 1 July (table S4). The rest of the top 5 years included 2013 (131 km^3; 21%), 1987 (95.8 km^3; 18%), 1986 (77.2 km^3; 15%), and 2014 (74.4 km^3; 11%). Comparatively, 1983 had a mean seasonal total melt potential contributed by snow-eater heat waves of 15.4 km^3 (or 6% of the seasonal total melt potential between 19 March and 1 July). For the overlapping SNOTEL record with 20CRv3 (1980–2015), the climatological mean total melt potential estimates within WUS mountainous regions ranged between 376 ± 58 km^3 (NHH) and 387 ± 65 km^3 (AHH). For context, Fang *et al.* (*41*) showed that WUS gridded observationally constrained SWE products had a climatological (1985–2021) mean peak SWE between 210 and 340 km^3. If accumulation season melt is also included, then WUS-wide climatological mean peak SWE estimates are closer to 400 km^3.

Figure 4 shows that all 20CRv3–SNOW-17 identified snow-eater heat-wave event duration and mean WUS-wide mountainous region

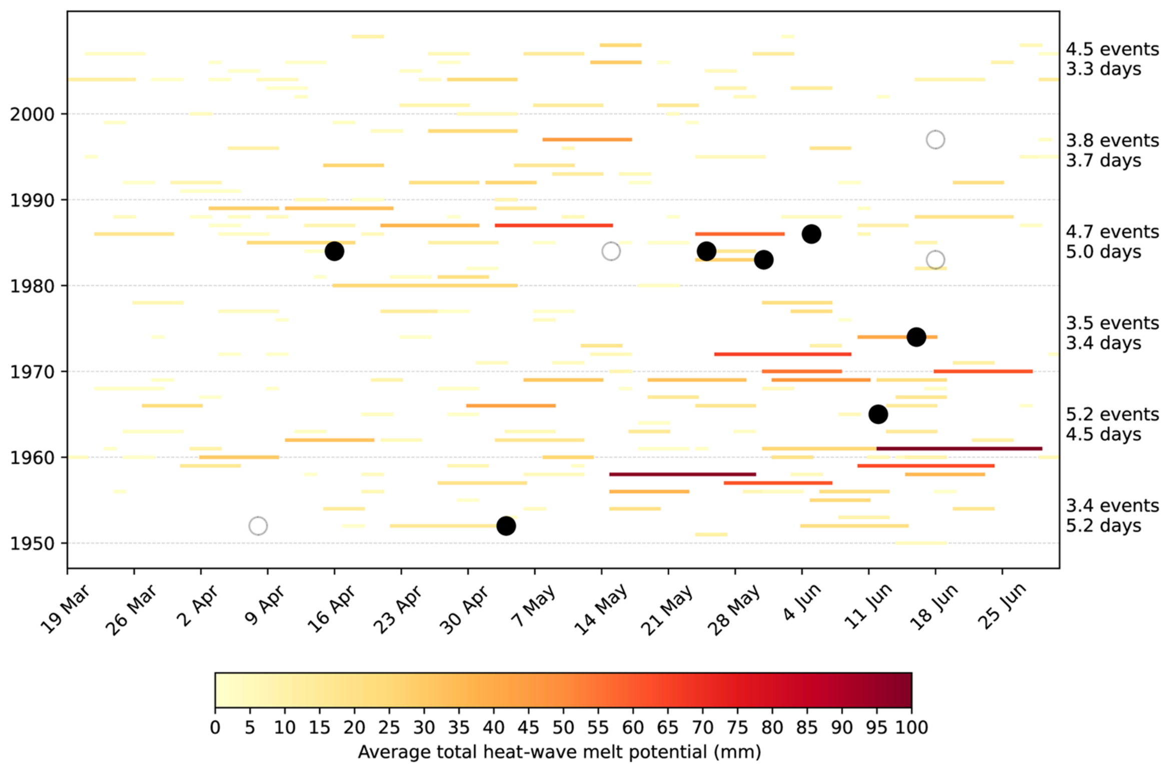

Fig. 4. Climatological (1950–2010) catalog of snow-eater heat-wave event frequency, duration, and modeled melt potential. A catalog of 20CRv3–SNOW-17 defined snow-eater heat-wave events between 1950 and 2010. Each line represents a unique snow-eater heat-wave event identified anywhere within the WUS mountainous regions. Each line length represents the snow-eater heat-wave event duration, and the line colors represent the area average cumulative total snow-eater heat-wave melt potential over its duration derived from the NHH SNOW-17 model. Overlaid dots represent the 11 spring-season, snowmelt-induced superflood events identified by Tarouilly *et al.* (*3*). If an 20CRv3–SNOW-17 identified snow-eater heat-wave event falls within 5 days of the superflood events identified by Tarouilly *et al.* (*3*), then a black dot is provided, else a hollow circle. The decadal annual average snow-eater heat-wave event frequency and durations are provided on the right *y* axis.

daily melt potential intensity between 1950 and 2010, which is the same corresponding period used by Tarouilly *et al.* (*3*). A complete catalog from 1850 to 2015 is provided in fig. S8. Decadal annual average snow-eater heat-wave event frequency and duration ranged between 3.4 and 5.2 events and 3.3 and 5.2 days per year, respectively, between 1950 and 2010. The dots on the plot represent the 11 spring superflood events that were identified and predominantly driven by snowmelt (rather than rainfall only or rain on snow). There is high correspondence between our 20CRv3–SNOW-17–based snow-eater heat-wave event identifications and the superfloods identified by Tarouilly *et al.* (*3*), with 7 of the 11 superflood events occurring within 5 days of our 20CRv3–SNOW-17–identified snow-eater heat-wave events. Even in the years in which a spring, snowmelt-induced superflood was identified, our snow-eater heat-wave event methodology identified most of the events, such as in 1983 (one of the two snowmelt superflood events were identified; Fig. 2) and 1984 (two of the three snowmelt superflood events were identified; fig. S9). The only year in the SNOTEL period of record in which a complete mismatch occurred between the 20CRv3–SNOW-17 snow-eater heat-wave identification and the Tarouilly *et al.* (*3*) superflood catalog was in 1997 (fig. S10). In that year, the 20CRv3–SNOW-17 methodology identified mid-May as the snow-eater heat wave event occurrence, whereas Tarouilly *et al.* (*3*) identified a superflood event in mid-June.

Preindustrial to present-day trends in snow-eater heat-wave characteristics

Given the high correspondence between our 20CRv3–SNOW-17 estimates of snow-eater heat waves and their melt potential compared with SNOTEL observations of dSWE and close proximities between snow-eater heat-wave occurrences with spring, snowmelt-dominated superfloods identified by Tarouilly *et al.* (*3*), we next explore how snow-eater heat-wave characteristics (e.g., area, duration, and frequency) have changed across WUS mountains since the 1850s. Compared to the preindustrial period of 1850–1899, T2m has a negligible mean trend (Mann-Kendall P value of 0.408 and Theil-Sen trend of −0.041 per century; fig. S15A). Despite a negligible mean trend in 20CRv3-derived spring T2m, the T2m freezing area in WUS mountainous areas has shown a steady decline since the 1850s (fig. S15B). Because above-freezing temperatures for 3 consecutive days (both day and night) are a snow-eater heat-wave criterion, any decreases in T2m freezing area should increase snow-eater heat-wave area. The area of snow-eater heat waves has increased, on average, by 102,000 km^2 per century across WUS-mountainous regions (Fig. 5A). In addition, snow-eater heat-wave frequency has increased by close to one event per century (Fig. 5C). The increase in snow-eater heat-wave events could be due to the erosion of the freezing level area in WUS-mountainous regions earlier in the late winter to early spring (e.g., March). This is corroborated by our 20CRv3-based results that the month of the first snow-eater heat-wave occurrence happens a month earlier per century between March and July (Fig. 5B). However, snow-eater heat-wave durations have decreased by half a day since the 1850s (Fig. 5D). As shown in fig. S8, the 50-year annual average number of snow-eater heat-wave events and their durations vary from 3.0 events that last 5.0 days (between 1850 and 1900) to 4.1 events that last 4.3 days (1950–2000). Duration decreases could be due to increases in the peripheral snow-eater heat-wave event areas (that occur for shorter durations), which then influence the area mean duration estimates.

Although many snow-eater heat-wave characteristics between 19 March and 1 July have appreciably changed since the 1850s (i.e., area, duration, frequency, and month of first occurrence), snow-eater heat-wave total melt potential intensity shows a weaker signal (Fig. 6A). This is likely influenced by average T2m trends in WUS mountainous regions showing a variable, yet nearly zero trend since the 1850s (fig. S15A). Regardless of the 20CRv3–SNOW-17 model used, snow-eater heat-wave total melt potential intensity across WUS mountainous regions increases (Theil-Sen trend that ranges between +0.93 and +1.94 km^3 per century based on the 20CRv3–SNOW-17 model used). The increase in snow-eater heat wave–only total melt potential intensity is evenly distributed between both daytime and nighttime (Fig. 6, C and D), likely shaped by our criterion that snow-eater heat-wave conditions be maintained through the daytime and nighttime. While these snow-eater heat wave–only total melt potential intensity trends are positive, they are also marked by substantial interannual variability. Changes in snow-eater heat-wave characteristics (e.g., area and duration) and systemic T2m biases in 20CRv3 likely shaped melt potential trends.

Across the three 20CRv3–SNOW-17 melt potential models, the average and 90th percentile WUS mountainous region snow-eater heat wave–only total melt potential from 1850 to 2015 was 47 and 125 km^3, respectively, which represents 10 and 22% of the total seasonal melt potential contribution, respectively (Fig. 6B). The anomalous WUS drought conditions of the 1850s and 1860s (*42*, *43*), or what has been termed the "Civil War drought," had some of the largest snow-eater heat wave–only total melt potential intensity estimates (table S5), with the largest occurring in 1869 (*44*), the year in which J. W. Powell began his exploration of the WUS and its water resources. On the basis of which of the 20CRv3–SNOW-17 models are used, the total snow-eater heat wave–only melt potential contribution between 19 March and 1 July of 1869 was 196 to 341 km^3 or 35 to 45% of the total seasonal melt potential (table S6).

We now explore whether snow-eater heat-wave melt potentials have changed on daily (Mx1day) and multiday perspectives (Mx3day and Mx5day) between 19 March and 1 July across 1850 to 2015. Figure 7A shows how snow-eater heat wave–only Mx1day trends since the 1850s have increased by 1.55 to 2.53 km^3 per century (based on the use of NHH, HH, or AHH). This same positive trend also holds for snow-eater heat wave–only Mx3day and Mx5day (Fig. 7, B and C). Mx3day has increased more (+2.35 to +4.20 km^3 per century) than Mx5day (+1.51 to +3.29 km^3 per century). The largest snow-eater heat wave–only Mx5day season occurred in 2014 with estimates of 84.2 to 122 km^3, based on which 20CRv3–SNOW-17 model is used (table S7). Notably, Mx1day, Mx3day, and Mx5day trends are all marked by large interannual variability between 1850 and 2015.

DISCUSSION

Snow-eater heat waves have received little research attention; however, these events play a crucial role in shaping WUS snowmelt patterns, particularly in the spring and early summer. For example, in late May of 1983, a 5-day snow-eater heat-wave event occurred, coinciding with the largest spring season, snowmelt-dominated superflood event in modern WUS history (*3*). Notably, this superflood occurred in large part due to the above normal snow accumulation before the snow-eater heat-wave event occurrence. We devised a methodology to identify, track, and estimate the melt potential (the

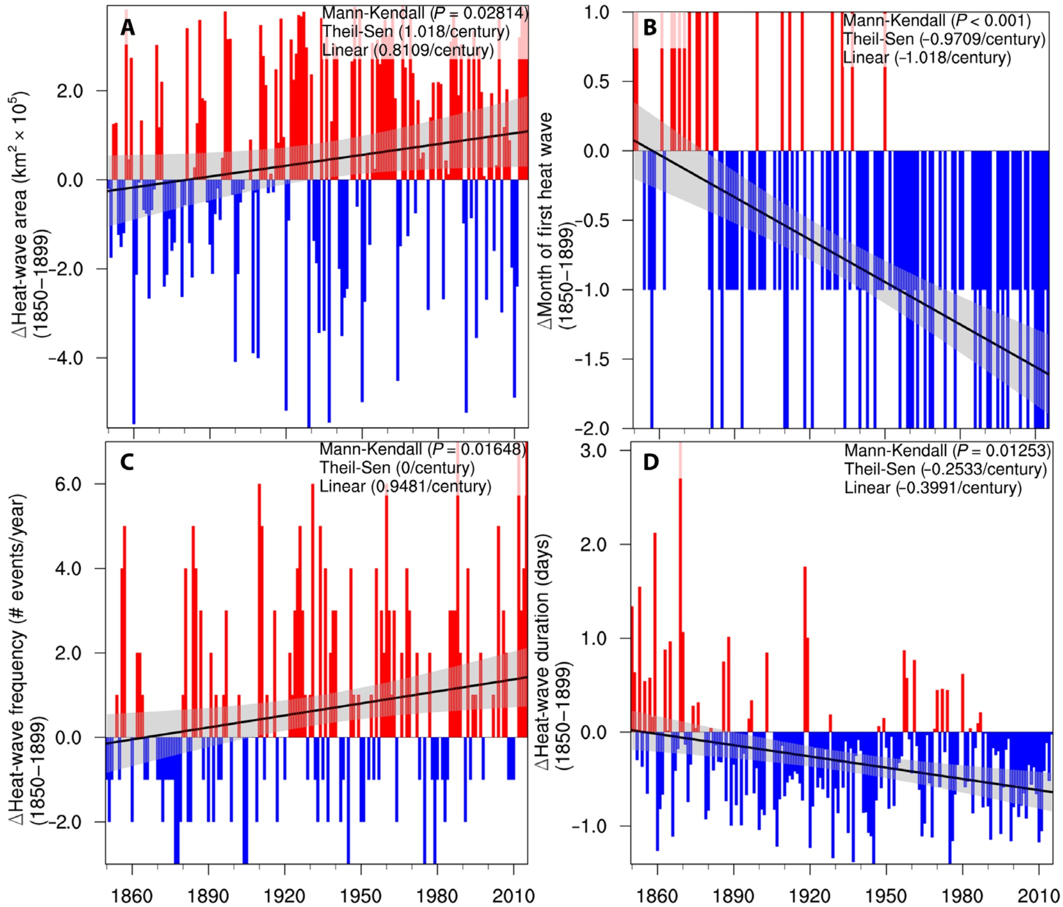

Fig. 5. Snow-eater heat-wave area, seasonality, frequency, and duration changes since the preindustrial period. Seasonal (19 March to 1 July) anomalies in 20CRv3-derived snow-eater heat-wave (**A**) area, (**B**) month of first occurrence, (**C**) frequency, and (**D**) duration from 1850–2015 over WUS mountainous regions relative to a 1850–1899 climatology. The solid black line indicates the ensemble mean linear regression trend, with gray shading representing the 95% confidence interval of the linear regression fit. The Mann-Kendall trend *P* values, Theil-Sen slope, and linear trend slope values are provided at the top of each subplot.

maximum amount of SWE that could melt if it existed) of WUS snow-eater heat-wave events, using the 11 spring, snowmelt-dominated superflood events (e.g., 1983) as a litmus test of our workflow. Our methodology was developed with a use-inspired goal as it can be applied to any observational or gridded product that provides daily-to-subdaily T2m and leverages a widely used, operational snowmelt model (SNOW-17) to estimate snow-eater heat-wave melt potentials. The melt potentials produced by this operational model were assessed using an out-of-the-box version and several experimental versions that enhance melt potential during snow-eater heat-wave events.

By using T2m estimates from the 20CRv3 product, we assessed how certain snow-eater heat-wave characteristics have (or have not) notably changed between 1850 and 2015. Our study highlights several key findings about 19th to 21st century WUS snow-eater heat-wave characteristics:

1) SNOTEL observations of dSWE on snow-eater heat wave–only days have nearly twice as much melt (−17 mm/day) compared to all melt days (−9.0 mm/day) across 1980–2015. This increased melt on snow-eater heat-wave days also occurs in more extreme moments of melt distributions (e.g., 90th percentile dSWE days enhance observed melt from −28 mm/day on all days to −36 mm/day on snow-eater heat wave–only days).

2) The 20CRv3–SNOW-17 methodology represents mean melt potential well on all days (−11 mm/day) and snow-eater heat wave–only days (−22 mm/day) compared to SNOTEL-observed −dSWE on those days.

3) Without enhanced melt on snow-eater heat-wave days, 20CRv3–SNOW-17 melt potentials underestimate extreme melt days in SNOTEL observations (i.e., 90th and 99th percentile −dSWE days). We introduce experimental 20CRv3–SNOW-17 models that better account for extreme melt potential on snow-eater heat-wave days, although with concomitant degradation in mean daily melt potential performance.

4) Since the 1950s, annual average snow-eater heat-wave event counts were 3 to 5 events/year, lasting 3 to 5 days each. We show that seven of the 11 spring season snowmelt-dominated superfloods identified by Tarouilly *et al.* (*3*) can be linked in close temporal proximity to snow-eater heat-wave events. This includes the largest event (since the 1950s), which lasted 5 days in late May 1983.

5) Since the 1850s, snow-eater heat-wave event areas have increased (+102,000 km^2 per century), durations have decreased (−0.25 day per century), frequencies have increased (+1 event per century), and the month of first occurrence has shifted earlier (−1 month per century) in WUS mountains. These linear estimates may underestimate rates of change in recent or future decades.

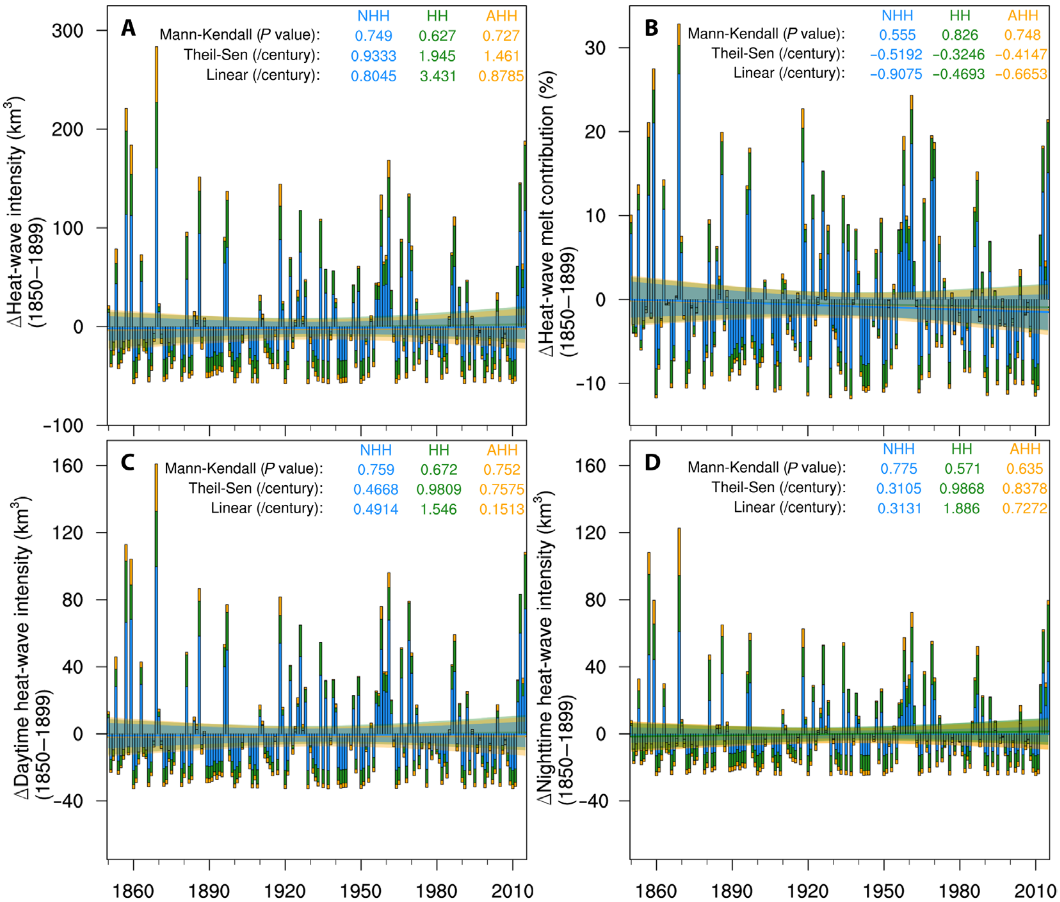

Fig. 6. Snow-eater heat wave modeled melt potential intensity changes since the preindustrial period. Seasonal (19 March to 1 July) anomalies in 20CRv3-derived snow-eater heat-wave average (**A**) total heat-wave intensity, (**B**) contribution of heat-wave melt days to total seasonal melt, (**C**) total daytime intensity, and (**D**) total nighttime intensity from 1850–2015 over WUS mountainous regions relative to a 1850–1899 climatology. Daytime and nighttime estimates of intensity are computed by converting 20CRv3–SNOW-17 melt potential estimates into local time and then accounting for time zone offsets (every 15° of longitude), solar declination, and hour angle at sunrise/sunset. Colors represent different 20CRv3–SNOW-17 models, including blue (NHHs), green (HHs), and orange (AHHs). Solid colored lines indicate the ensemble mean linear regression trend for each model, with shaded regions of the corresponding color representing the 95% confidence interval of the linear regression fit. The Mann-Kendall trend *P* values, Theil-Sen slope, and linear trend slope values for each 20CRv3–SNOW-17 model are provided at the top of each subplot.

6) Between 1850 and 2015, the top 25 snow-eater heat wave contributed melt seasons ranged between 14 and 45% of the 19 March to 1 July total seasonal melt potential.

7) Melt potential rates, whether from the perspective of total seasonal melt potential, Mx1day, Mx3day, and Mx5day, show a positive trend since the 1850s. However, these trends are also marked by large interannual variability.

We next present the main sources of uncertainty in the study. These include the differences between potential melt and actual snowmelt, the limitations of temperature index models, and the use of the 20CRv3 reanalysis T2m estimates. We also highlight future work that could be pursued to advance snow-eater heat-wave understanding.

Melt potential is not actual snowmelt. This difference is analogous to the limitations of potential evapotranspiration compared with actual evapotranspiration (*45*). Melt potential thus represents an upper bound of the amount of possible snowmelt if sufficient snow accumulated in the weeks to months before a given snowmelt event. This important discrepancy was shown in our top 25 years of total seasonal melt potential, with several of the top years corresponding with well-documented snow droughts, such as 2013–2015 in California (*46*, *47*). This is especially true during snow-eater heat-wave events, as the potential for melt can only be realized if this same amount of snow exists. For example, the antecedent snow conditions combined with a snow-eater heat-wave event in late May 1983 resulted in the largest spring season, snowmelt-dominated superflood event in modern WUS history (*3*).

Temperature index snow models, such as SNOW-17, are the standard approach at operational forecasting centers due to their reliance on a single variable (T2m) that is more widely accessible across WUS mountains, their computational efficiency, and their simplicity that helps in describing causality (*48*). However, temperature index snow models do not represent all snow-atmosphere couplings (*49*, *50*) or the full suite of energy balance contributions to snowmelt. For example, downwelling solar radiation (*51*), snow albedo (*52*, *53*), relative humidity (*54*), snowfall intensity (*55*), and rain-on-snow events (*19*) affect WUS spring and summer snowmelt rates. These snow-atmosphere interactions could enhance or diminish the

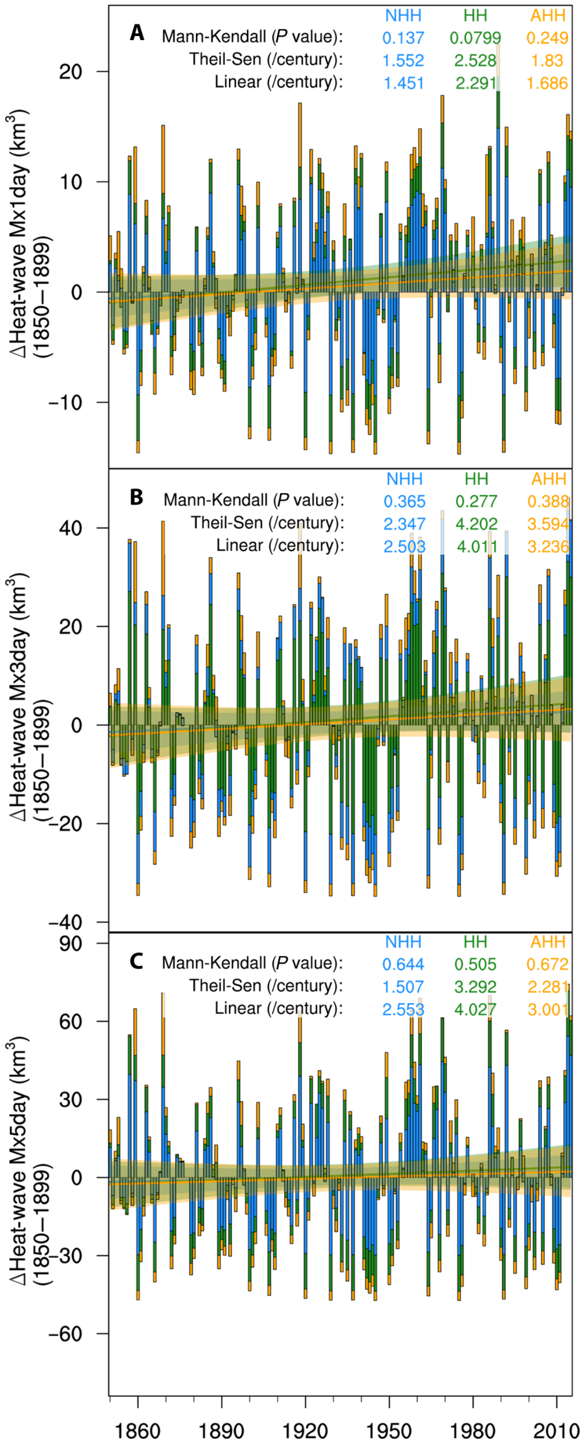

Fig. 7. Snow-eater heat wave modeled extreme melt potential intensity changes since the preindustrial period. (**A**) Mx1day, (**B**) Mx3day, and (**C**) Mx5day anomalies in 20CRv3–SNOW-17–derived snow-eater heat-wave total intensity between 19 March and 1 July from 1850 to 2015 over WUS mountainous regions relative to a 1850–1899 climatology. Colors represent different 20CRv3–SNOW-17 models, including blue (NHHs), green (HHs), and orange (AHHs). Solid colored lines indicate the ensemble mean linear regression trend for each model, with shaded regions of the corresponding color representing the 95% confidence interval of the linear regression fit. The Mann-Kendall trend *P* values, Theil-Sen slope, and linear trend slope values for each 20CRv3–SNOW-17 model are provided at the top of each subplot.

potential for extreme snowmelt, which, in turn, influences flood and water supply forecasting.

Future work could contrast snow-eater heat-wave events represented in temperature index versus mass-energy balance snow models to see how these snow-atmosphere feedbacks enhance or diminish extreme snowmelt. Furthermore, temperature index models do not partition snow ablation into sublimation and melt, which could have contributed to some of the mismatches we found between our snow-eater heat-wave catalog and WUS superflood event occurrences. For example, a snow-eater heat-wave event may have sublimated rather than melted the snowpack, leading to no streamflow response. Enhanced sublimation would be particularly evident during hot and dry snow-eater heat-wave events, which warrants further work. Alternatively, earlier season melt and/or rainfall events may have elevated soil moisture, leading to more efficient runoff later in the season (*56*). Further, rain-on-snow events that occur before, rather than coincident with (as was explored in this study), a snow-eater heat-wave event may differentially influence snowpack ripening and snowmelt rates (*57*). Future work could investigate the effects of antecedent conditions before snow-eater heat-wave events, and how other snow-atmosphere couplings and mass-energy balance fluxes amplify and/or diminish snow-eater heat wave–driven ablation, such as comparing pre- and postwildfire ablation responses during snow-eater heat-wave events (*53*, *58*).

The 20CRv3 reanalysis dataset offers a valuable long-term, ensemble-based atmospheric dataset, with global coverage, at a subdaily temporal frequency. However, its reliance on surface pressure-only assimilation and lack of direct snowpack or temperature observations introduces uncertainties, particularly for assessing high-resolution snowmelt dynamics and snow-eater heat-wave events in the varied geographies of the WUS. For example, between 1851–1900 and 2005–2014, 20CRv3 estimates have a cooler spring T2m warming pattern over North America (+1.19 K) compared to Berkeley Earth, Climatic Research Unit, and the Global Historical Climatology Network (+1.33 K), particularly in May (*59*, *60*). These spring T2m trend discrepancies could partly be attributed to our evaluation of trends within only WUS mountainous regions , where WUS low-lying areas have shown stronger spring warming trends due to more frequent, warm maritime air intrusion (*61*). In addition, while the 20CRv3 development team has continued to make adjustments to the data from 1850 to 2015, the dataset is not currently being updated forward in time, meaning that it cannot be used to assess potential shifts in snow-eater heat-wave characteristics over the most recent decade, which includes some of the hottest years ever recorded (*1*, *62*), nor in a real-time forecasting context. Continually updating ERA5 (the fifth generation of the European Centre for Medium Range Weather Forecasts reanalysis) and/or Integrated Forecasting System (IFS) products could provide a path forward for contemporary analysis (see the Supplementary Materials for ERA5–SNOW-17–based results for 1980–2015). An additional advantage of using ERA5's T2m estimates is that it would allow for the use of ERA5-Land's skillful snowpack estimates (*63*) that could help to further constrain snow-eater heat-wave event identifications based on the presence of snow.

Given the identified size and potential impact on water resources and natural hazards, additional work on snow-eater heat-wave events is needed. We envision that this work could include the testing of the newly developed SNOW-17 experimental melt potential models in a real-time forecasting context, exploring subseasonal-to-seasonal predictability of snow-eater heat-wave events with large-scale modes of climate variability and identifying how different climate scenarios and/or warming levels could alter snow-eater heat-wave characteristics in the WUS (and other global mountainous regions) through the 21st century. In addition, the use of multiple T2m anomaly thresholds could be leveraged to develop a snow-eater heat-wave index. For example, moderate (+4 K), extreme (+6 K), and exceptional (+8 K) snow-eater heat-wave conditions. Our sensitivity analysis in the Supplementary Materials suggests that the identification of snow-eater heat waves and their relative melt intensity is robust to the threshold choice of +4 to +8 K (from a 1981–2010 base period), while their spatial extents would vary (figs. S11 and S12).

Results in this study suggest that it may be beneficial to adopt different SNOW-17 parameterizations during snow-eater heat-wave and non–heat wave events, analogous to what is done for rain-on-snow events already in SNOW-17 in equation 6 of Anderson *et al.* (*39*, *64*). Our snow-eater heat-wave identification strategy and newly developed additive melt term during snow-eater heat-wave events help SNOW-17 to better represent extreme melt potential estimates (i.e., 90th to 99th percentiles) compared to observed − dSWE at SNOTEL sites. Therefore, we envision that T2m estimates from real-time weather forecasts (e.g., IFS) could be leveraged with our newly developed SNOW-17–based probabilistic framework during snow-eater heat-wave events to estimate the cone of uncertainty of plausible extreme melt potentials. The goal of this cone of uncertainty would be to better bracket extreme melt potentials and provide reservoir operators and flood planners with more information to make decisions as snow-eater heat-wave events develop and persist.

The ability to predict the area, duration, frequency, and/or intensity of snow-eater heat-wave events at subseasonal to seasonal timescales could also be worth exploring in future work (*65*). Operational modeling centers could benefit from a better understanding of the predictability of various snow-eater heat-wave event characteristics at subseasonal-to-seasonal timescales, particularly for snowmelt prediction and flood early warning. To do this, we envision that composite (*66*) and cluster-based analyses (*67*, *68*) could be used with our snow-eater heat-wave catalog to identify the large-scale meteorological patterns that give rise to snow-eater heat-wave events. The large-scale meteorological patterns could then be used in combination with information about their frequency and persistence under different climate modes of variability, for example, the El Niño Longitude Index (*69*), to identify the likelihood that a given season might have an increased or decreased chance of a snow-eater heat-wave occurence. Reservoir operators and flood planners could combine this information with seasonal forecasts of precipitation (*70*) to estimate the potential risk profile of both an accumulation of an abundant snowpack, combined with the potential for more snow-eater heat-wave events.

The flexibility of the reported snow-eater heat-wave identification framework should be extensible to other global mountain regions. Therefore, snow-eater heat-wave characteristic changes over the past two centuries could be derived and intercompared across mountains (*71*) and snow climates (*72*) to derive a flood potential index, analogous to the water tower index (*73*). Similar to what occurred in the Pacific Northwest in 2021 during a snow-eater heat wave–like event (*1*, *74*), rapid glacier and seasonal melt during heat-wave events has also been observed in the European Alps (*75*) and South American Andes (*76*, *77*). The increasing trends in snow-eater heat-wave area and frequency, combined with an earlier timing in the spring season, warrant further investigation into the middle and latter portions of the 21st century under different, plausible warming trajectories (*78*). There is strong evidence that seasonal snowpacks will diminish substantially by the end of the century, such as those in the American Cordillera (*25*, *26*, *79*). However, between the present decade and the middle of the 21st century, snow-eater heat wave–induced flooding likelihoods could peak before declining into the end of the 21st century, analogous to the concept of peak rain-on-snow introduced by Heggli *et al.* (*80*). This highlights the relevance and urgency to continue studying heat-wave impacts on snow and their predictability at relevant timescales for resource and emergency management.

MATERIALS AND METHODS

The workflow developed to identify snow-eater heat-wave characteristics between the 19th and 21st centuries is summarized in Fig. 8. Subsequent subsections and the Supplementary Materials provide additional information about methodological assumptions and choices made in this workflow.

Snow-eater heat-wave identification and tracking

Our end-to-end workflow can be applied to any gridded dataset that provides subdaily-to-daily T2m estimates. We chose to use the 20CRv3 (*36*–*38*) as it provides a long spatiotemporally continuous meteorological dataset. 20CRv3 is a gridded (~75-km grid spacing) estimate of atmospheric and land surface conditions that spans 1806 to 2015. To constrain its model-based estimates of atmospheric and land surface conditions, 20CRv3 assimilates surface observations of surface air pressure and prescribes lower boundary conditions of sea surface temperature and sea ice concentrations. 20CRv3 leverages an ensemble-based data assimilation system to produce an 80-member ensemble that accounts for three forms of uncertainty: internal climate variability, observational, and structural.

We leverage 3-hourly estimates of T2m to identify and estimate the melt potential (i.e., potential melt rates if snowpack exists) of snow-eater heat waves from 1850 to 2015 (defined and discussed in subsequent sections). We opted to use data beginning at 1850 onward since the data from 1806 to 1835 is experimental and might lead to trend analysis inconsistencies with data post-1835. This also coincides with the Intergovernmental Panel on Climate Change's preindustrial period (1850–1899) and is the earliest period at which observations were near-global (*81*). The spatial bounds of the WUS in our study span 30 to 50 N by −124 to −104 W. Within this region, there are a total of 812 grid cells in 20CRv3.

Slivinski *et al.* (*38*) found that 20CRv3 demonstrates comparable 3- to 4-day forecast skill as operational forecasting models (circa 2019) when estimating 500-hPa geopotential height fields over the near-term period of 1979–2015. This provides confidence that it skillfully represents mid-tropospheric atmospheric circulation patterns, particularly during the mountainous WUS observational record that overlaps with 20CRv3 (1980–2015). Nolin *et al.* (*59*) showed that 50-year climatological March to May T2m anomaly sign and spatial extent over North America in 20CRv3 correlated strongly with the Berkeley Earth and a tree ring–based paleoclimate reconstruction but with a cool bias.

We use 80-member ensemble mean 3-hourly T2m estimates to identify snow-eater heat-wave events using the following criteria:

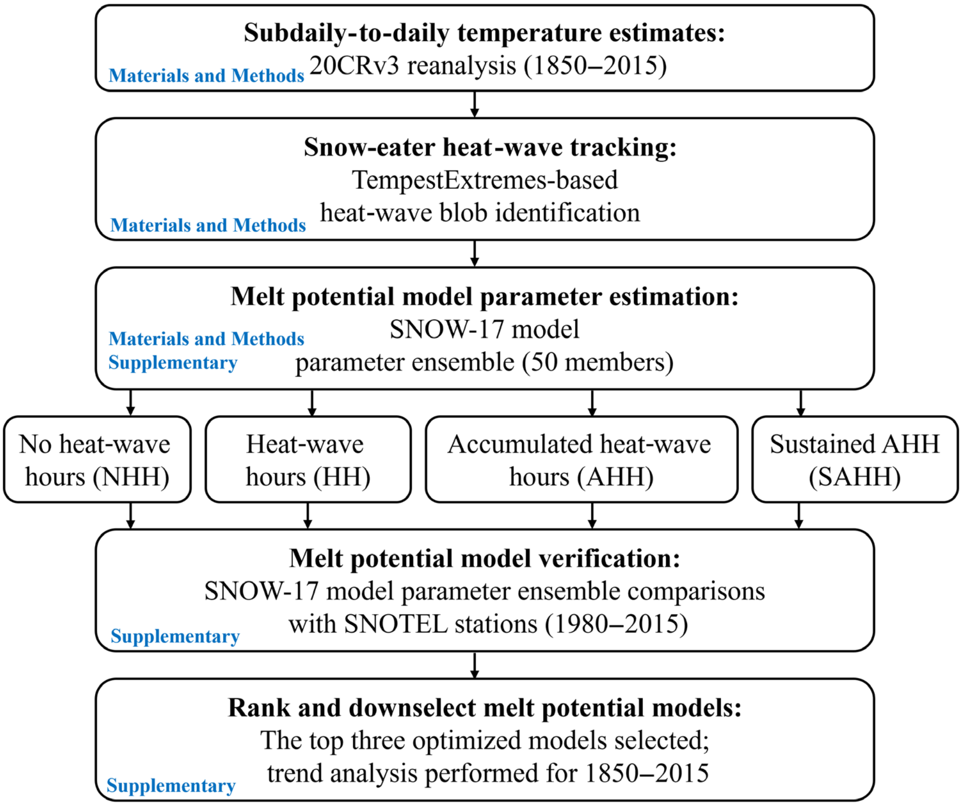

Fig. 8. Snow-eater heat-wave event identification, melt potential estimation, and verification workflow. The end-to-end workflow to identify snow-eater heat-wave events, estimate their melt potentials, and assess trends in their characteristics. The blue text indicates the subsections of the manuscript where specific details about the workflow can be found.

1) The event must occur after 19 March (spring equinox) and before 1 July.

2) The T2m must be above freezing.

3) Analogous to Reyes and Kramer (*1*), a T2m anomaly of +6 K should occur relative to a 3-hourly background climatology (1981–2010). The climatology is derived from day of year and time of day.

4) Criteria 2 and 3 are sustained for at least 3 days.

We selected these criteria for the following physical reasons: First, we sought to isolate events that occur when snowpacks approach their climatological peak and begin to melt out (19 March to 1 July). Second, as sudden shifts in T2m would not be expected to result in rapid melt if daily average T2m remains below freezing, we want to ensure that the snowpack experiences sustained above-freezing conditions that could lead to ripening and/or ablation. Third, the criteria further isolate anomalous T2m conditions that are not simply part of the normative transition between spring and summer. Last, we want to ensure that these conditions are sustained for a prolonged period [e.g., at least 3 days; a common heat-wave duration definition (*24*)] that accounts for a continuous and anomalous energy transfer from the atmosphere to the snowpack that depletes snowpack cold content, leading to snowmelt. Unfortunately, consistent cold content measurements at daily frequency (particularly across the WUS) are nonexistent. Therefore, to be reasonably conservative, we followed standard definitions used in other heat-wave literature as a starting point to develop our criteria. However, we suggest the refinement of the necessary and sufficient duration of the snow-eater heat-wave conditions mentioned above as future work.

To isolate regions of snow-eater heat waves in time and space, we use several CDOs (Climate Data Operators) (*82*), and the TempestExtremes StitchBlobs algorithm (*83*). CDO isolates the snow-eater heat-wave conditions to generate binary (0 or 1) spatiotemporal masks. StitchBlobs is then applied to these binary masks to identify distinct snow-eater heat-wave events and assign them specific identifiers. For example, the StitchBlobs flag minsize and mintime are set to 100 grid cells and 24 hours, respectively, to assign specific identifiers to each snow-eater heat-wave binary mask based on spatial and temporal overlap assumptions. minsize represents the minimum number of grid points per time slice for a given areal feature to be counted as a distinctly identified feature. mintime represents the minimum number of time slices for a given tracked areal feature to overlap with another areal feature at a prior time step to be counted as a distinctly identified areal feature. This workflow allows us to generate a historical catalog of events.

Snow-eater heat-wave melt potential

To provide a more decision-relevant assessment of how snow-eater heat-wave characteristics have changed since the 19th century, we use an operational snowmelt model. The operational snow accumulation and ablation model we leverage is SNOW-17, a conceptual model currently used by the National Weather Service (*39*). SNOW-17 requires T2m and precipitation as inputs, while snowmelt and SWE are outputs (84). SNOW-17 uses T2m as a proxy for energy exchange across the snow-air interface and applies empirically based relationships to compute snowpack heat storage, snowmelt, liquid water retention, and meltwater transmission (64, 84).

To quantify the melt potential of snow-eater heat waves and assess the fidelity of SNOW-17 in estimating both mean and extreme melt potential, we use the temperature index nonrain melt model within the SNOW-17 model [see equation 6 in Anderson *et al.* (39, 64)]. Temperature index models do not explicitly account for all surface radiative budget terms (e.g., net solar radiation) but instead rely on the strong relationship of snow-longwave radiation feedbacks (85) and a few parameters that attempt to account for aspect, slope, length of day, and land surface cover (discussed later). Temperature index models are also practical (i.e., only require estimates or observations of T2m), computationally efficient, and widely used in operational forecasting (48).

The SNOW-17 nonrain melt potential (M_{nr}) is defined as

$$M_{\mathrm{nr}}\left[d, \mathrm{MF}_{\min}, \mathrm{MF}_{\max}, \mathbf{T}_{\mathrm{a}}(d), \mathrm{MBASE}\right] = \sum_{h\in d} M_{\mathrm{f}}\left(d, \mathrm{MF}_{\min}, \mathrm{MF}_{\max}\right) * \left[T_{\mathrm{a}}(h) - \mathrm{MBASE}\right] \tag{1}$$

where d denotes the day of the year between 19 March and 1 July, $h = [0, 3, \ldots, 21]$ denotes the hour of d at 3-hour intervals, $\mathbf{T}_{\mathrm{a}}(d) = \{T_{\mathrm{a}}(d, h): h = 0, 3, \ldots, 21\}$ is a length-8 vector of T2m (in kelvin) provided by the 20CRv3 reanalysis dataset at 3-hourly resolution, MBASE denotes the baseline melt temperature (equal to 273.15 K), and $M_{\mathrm{f}}(d)$ is the seasonal variation in the nonrain melt factor (in millimeters per hour). Melt potential is only realized if the same amount of snow is present on the landscape. Therefore, melt potentials represent upper-bound estimates of actual snowmelt, analogous to the difference between actual evapotranspiration and potential evapotranspiration (45).

The seasonal variation, which accounts for the influence of the seasonal cycle of solar radiation and land surface feedbacks on melt potential, is defined as

$$M_{\mathrm{f}}\left(d, \mathrm{MF}_{\min}, \mathrm{MF}_{\max}\right) = S_{\mathrm{v}}(d) * A_{\mathrm{v}}(d) * \left(\mathrm{MF}_{\max} - \mathrm{MF}_{\min}\right) + \mathrm{MF}_{\min} \tag{2}$$

where $S_{\mathrm{v}}(d)$ accounts for solar variation based on the season, $A_{\mathrm{v}}(d)$ accounts for angular variation (i.e., latitude and time of year), and $\mathrm{MF}_{\min} < \mathrm{MF}_{\max}$. $\mathrm{MF}_{\min}$ and $\mathrm{MF}_{\max}$ account for local radiative and temperature effects on snowpack (e.g., south-facing versus north-facing slopes and forest cover types) as defined in a NOAA National Weather Service technical manual for SNOW-17 (86). More specifically, Table 1 in the NOAA NWS technical manual for SNOW-17 (86) states that for coniferous forests, $\mathrm{MF}_{\max}$ ($\mathrm{MF}_{\min}$) should range between 0.5 and 0.8 (0.2 and 0.3), whereas in open areas, $\mathrm{MF}_{\max}$ ($\mathrm{MF}_{\min}$) should range between 1.3 and 2.0 (0.5 and 0.9). Traditionally, these parameters are chosen by the user based on local knowledge of the region of interest (e.g., land surface cover). Across the WUS, $A_{\mathrm{v}}(d)$ is equal to 1.0 based on guidance in Anderson *et al.* (64). The solar variation $S_{\mathrm{v}}(d)$ accounts for the length of day (which influences radiative and temperature feedback on snowpack) and is defined as

$$S_{\mathrm{v}}(d) = \frac{1}{2}\sin\left[\frac{2\pi \mathrm{N}(d)}{366}\right] + \frac{1}{2} \tag{3}$$

where $N(d)$ is the number of days (d) since the spring equinox (19 March).

To estimate melt potential across the WUS, we developed a statistical model to estimate plausible data-informed estimates of the SNOW-17 parameters. For the 19 March to 1 July period, $\mathrm{MF}_{\min}$ has a negligible impact on melt potential. Therefore, we focus our attention solely on $\mathrm{MF}_{\max}$ and keep $\mathrm{MF}_{\min}$ fixed to its upper bound (see the Supplementary Materials for more discussion). Our proposed statistical model relates in situ measurements of the dSWE provided by the SNOTEL Network with collocated gridded estimates of T2m from 20CRv3. The model is estimated in a Bayesian paradigm and produces WUS-wide estimates of the spatially varying $\mathrm{MF}_{\max}$ parameter. To estimate $\mathrm{MF}_{\max}$, we first estimate $\mathrm{MF}_{\max}$ for each year between 1980 and 2015, obtaining 3000 samples from the posterior distribution and discarding the first 1500 as burn-in. For all models, convergence is assessed graphically using a random subset of parameters and numerically using $\widehat{R}$, with no lack of convergence detected. Within 1980–2015, we use the particular year's estimated $\mathrm{MF}_{\max}$ to estimate melt potential. Outside of 1980–2015, to account for SNOTEL measurement network's spatiotemporal coverage uncertainty between 1980 and 2015 (and ensure that $\mathrm{MF}_{\max}$ is not fine-tuned for performance in any particular year), we perform a weighted average of the posterior draws of $\mathrm{MF}_{\max}$ across 1980–2015 at each grid cell to estimate melt potential. The weights are determined on the basis of the number of SNOTEL observations across the WUS in a given year (i.e., 8254 measurements in 1980 to 39,474 measurements in 2015). This results in 1500 posterior estimates of the WUS-wide spatially varying $\mathrm{MF}_{\max}$. Because of the computational cost of the subsequent analysis, we opt to retain 50 random draws from the posterior distribution of the $\mathrm{MF}_{\max}$ parameter to estimate melt potential, which we refer to as the ensemble of melt potential estimates. We found that a 50-member ensemble of SNOW-17 melt potential estimates was the optimal choice between balancing the representation of the underlying distribution of melt potential estimates and computational resources. The Supplementary Materials contains specific details of this parameter estimation.

In addition, we propose a natural log additive term to Eq. 1 that captures enhanced melt potential on snow-eater heat-wave days. This additive term can be scaled and varied in its melt strength based on a fixed parameter (k) and the snow-eater heat-wave presence and duration. The out-of-the-box and experimental versions of the SNOW-17 model were intercompared and ranked to identify the top three performing models over the SNOTEL period of record (1980–2015). These three melt potential models include the out-of-the-box SNOW-17 model, which has NHH influence, and two experimental models, HHs and AHHs. More details about these experimental models and their verification are provided in the Supplementary Materials.

Our hypothesis in devising an additive melt term in the SNOW-17 melt equation is based on several factors. During snow-eater heat waves, we anticipate that a snowpack would experience a prolonged period (both day and night) of elevated temperatures, yielding enhanced downwelling longwave and sensible heat fluxes (Fig. 1). In addition, we expect clear sky conditions, leading to an increase in downward shortwave radiation during the day. In certain circumstances, during prolonged high pressure and the presence of upper-level cirrus clouds (which can be advected into the region), enhanced downward longwave radiation can occur at night (87–89). The combination of these feedbacks could lead to sustained loss of cold content and enhanced snowmelt rates (90, 91).

WUS-wide estimates of MF_{max} for the 20CRv3–SNOW-17 NHH, HH, and AHH models can be found in fig. S1 (A to C). The 50-member ensemble mean, median, and maximum MF_{max} values used at any given 20CRv3 grid cell across the WUS are shown. Notably, there is a significant amount of spatial heterogeneity in the ensemble of MF_{max} values used across the three 20CRv3–SNOW-17 models. Therefore, a fixed MF_{max} value across the WUS would not have led to the best possible melt potential estimates.

We performed a sensitivity analysis of how snow-eater heat-wave identification criterion (i.e., 20CRv3-based T2m of +4 K versus +6 K versus +8 K above a 3-hourly background climatology, 1981–2010) and how reanalysis dataset choice [i.e., 20CRv3 versus ERA5, the fifth generation of the European Centre for Medium Range Weather Forecasts reanalysis (*92*), using a +6-K T2m anomaly above a 3-hourly background climatology, 1981–2010] shaped our results. We refer readers to the Supplementary Materials for more information.

Snow-eater heat-wave metrics

We compute several metrics to add context to the snow-eater heat-wave catalog. These metrics are computed across 19 March to 1 July and include the seasonal total melt potential, snow-eater heat wave contributed melt potential, and the maximum 1-, 3-, and 5-day melt potential (Mx1day, Mx3day, and Mx5day, respectively). The percent contribution of snow-eater heat-wave melt potential is computed by taking the melt on snow-eater heat wave–only days and dividing by the total melt potential across all days between 19 March and 1 July. To identify the top years for these metrics, we take the mean of the 50-member ensemble melt potential estimates, sum the melt potentials over all possible periods of interest (e.g., 5 days), spatially average those periods, find the maximum across all possible periods, and then convert those estimates from millimeters to cubic kilometers by multiplying the depth of melt potential by the area of the snow-eater heat-wave masks. The melt potential estimates can be computed in regions that do not typically have ephemeral or seasonal snowpacks (*93*). To limit this bias when we intercompare the melt potentials across years throughout the WUS, we mask the melt potential estimates with a widely used mountain mask developed by Körner *et al.* (*71*). Figure S1 provides outlines of these WUS mountainous regions. We also compare our catalog of snow-eater heat-wave dates and durations with the Tarouilly *et al.* (*3*) WUS top 100 superflood catalog. To assess trends in snow-eater heat-wave characteristics between 1850 and 2015, we compute spatial average seasonal anomalies within WUS mountainous regions, comparing each season to a 50-year preindustrial base period (1850–1899). The nonparametric Mann-Kendall and Theil-Sen tests are computed to assess the sign and associated *P* values of the trends (*94*).

Supplementary Materials

This PDF file includes:
Supplementary Text
Figs. S1 to S15
Tables S1 to S8
References

REFERENCES

1. L. Reyes, M. G. Kramer, High-elevation snowpack loss during the 2021 Pacific Northwest heat dome amplified by successive spring heatwaves. *npj Clim. Atmos. Sci.* **6**, 208 (2023).
2. S. I. Seneviratne, X. Zhang, M. Adnan, W. Badi, C. Dereczynski, A. Di Luca, S. Ghosh, I. Iskandar, J. Kossin, S. Lewis, F. Otto, I. Pinto, M. Satoh, S.M. Vicente-Serrano, M. Wehner, B. Zhou, "Weather and climate extreme events in a changing climate," in *IPCC 2021: Climate Change 2021: The Physical Science Basis. Contribution of Working Group I to the Sixth Assessment Report of the Intergovernmental Panel on Climate Change*, V. Masson-Delmotte, P. Zhai, A. Pirani, S.L. Connors, C. Péan, S. Berger, N. Caud, Y. Chen, L. Goldfarb, M.I. Gomis, M. Huang, K. Leitzell, E. Lonnoy, J.B.R. Matthews, T.K. Maycock, T. Waterfield, O. Yelekçi, R. Yu, B. Zhou, Eds. (Cambridge Univ. Press, 2021), pp. 1513–1766.
3. E. Tarouilly, D. Li, D. P. Lettenmaier, Western U.S. superfloods in the recent instrumental record. *Water Resour. Res.* **57**, e2020WR029287 (2021).
4. T. Arnow, *Water-Level and Water-Quality Changes in Great Salt Lake, Utah, 1847–1983* (US Department of the Interior, Geological Survey, 1984), vol. 913.
5. K. Lindskov, "Floods of May to June 1983 along the Northern Wasatch Front, Salt Lake City to North Ogden, Utah" (Tech. Rep. 10.3133/ofr84456, US Geological Survey, 1984).
6. B. J. Hatchett, S. Bacon, W. T. Brandt, A. Heggli, J. Lancaster, Snowmelt-triggered debris flows in seasonal snowpacks. *Int. Conf. on Debris Flow Hazard Mitig.* **415**, 1–4 (2023).
7. P. H. Burgi, in *1983 Flow Emergency at Glen Canyon Dam–The Fastest Boat through the Grand Canyon* (American Society of Civil Engineers, 2020), pp. 23–33.
8. D. J. McEvoy, B. J. Hatchett, Spring heat waves drive record western United States snow melt in 2021. *Environ. Res. Lett.* **18**, 014007 (2023).
9. E. Bercos-Hickey, T. A. O'Brien, M. F. Wehner, L. Zhang, C. M. Patricola, H. Huang, M. D. Risser, Anthropogenic contributions to the 2021 Pacific Northwest Heatwave. *Geophys. Res. Lett.* **49**, e2022GL099396 (2022).
10. A. Shabbar, B. Bonsal, An assessment of changes in winter cold and warm spells over Canada. *Nat. Hazards* **29**, 173–188 (2003).
11. S. E. Perkins, L. V. Alexander, J. R. Nairn, Increasing frequency, intensity and duration of observed global heatwaves and warm spells. *Geophys. Res. Lett.* **39**, 20714 (2012).
12. M. Beniston, Warm winter spells in the Swiss Alps: Strong heat waves in a cold season? A study focusing on climate observations at the Saentis high mountain site. *Geophys. Res. Lett.* **32**, L01812 (2005).
13. R. R. Colucci, F. Giorgi, C. Torma, Unprecedented heat wave in December 2015 and potential for winter glacier ablation in the eastern Alps. *Sci. Rep.* **7**, 7090 (2017).
14. K. N. Musselman, N. Addor, J. A. Vano, N. P. Molotch, Winter melt trends portend widespread declines in snow water resources. *Nat. Clim. Change* **11**, 418–424 (2021).
15. X. Li, S. Wang, Recent increase in the occurrence of snow droughts followed by extreme heatwaves in a warmer world. *Geophys. Res. Lett.* **49**, e2022GL099925 (2022).
16. Y. Yang, Q. You, T. Smith, R. Kelly, S. Kang, Spatiotemporal dipole variations of spring snowmelt over Eurasia. *Atmos. Res.* **295**, 107042 (2023).
17. L. Scaff, S. A. Krogh, K. Musselman, A. Harpold, Y. Li, M. Lillo-Saavedra, R. Oyarzún, R. Rasmussen, The impacts of changing winter warm spells on snow ablation over Western North America. *Water Resour. Res.* **60**, e2023WR034492 (2024).
18. G. Deng, T. Zhang, X. Liu, Y. He, H. Chen, Q. Shen, Q. Chen, Z. Tang, Intensifying heatwave events affect snow phenology over the Tibetan Plateau. *J. Hydrol.* **659**, 133293 (2025).
19. G. J. McCabe, M. P. Clark, L. E. Hay, Rain-on-snow events in the western United States. *Bull. Am. Meteorol. Soc.* **88**, 319–328 (2007).
20. J. Welty, X. Zeng, Characteristics and causes of extreme snowmelt over the conterminous United States. *Bull. Am. Meteorol. Soc.* **102**, E1526–E1542 (2021).
21. A. Gershunov, B. Hatchett, A. Weyant, M. D. Dettinger, L. Su, A. Rhoades, P. Williams, P. Williams, M. L. Anderson, P. Rittelmeyer, D. Lettenmayer, D. R. Cayan, R. Luna-Niño, K. Guirguis, T. W. Corringham, R. Meandly, F. M. Ralph, Atmospheric rivers and floods in California's changing hydroclimate. *San Franc. Estuary Watershed Sci.* **23**, 10.15447/sfews.2025v23iss3art3 (2025).
22. F. Z. Maina, S. V. Kumar, Global patterns of rain-on-snow and its impacts on runoff from past to future projections. *Nat. Commun.* **16**, 4731 (2025).
23. Y. Zhou, M. M. Wehner, A. M. Rhoades, A. D. Jones, The role of wind-moisture characteristics in shaping atmospheric river flood hazards. *Geophys. Res. Lett.* **52**, e2025GL117548 (2025).
24. B. Disher, B. Edwards, T. Lawler, D. Radford, in *Measuring Heatwaves and Their Impacts* (Springer US, 2021), pp. 455–475.
25. E. Siirila-Woodburn, A. M. Rhoades, B. J. Hatchett, L. S. Huning, J. Szinai, C. Tague, P. S. Nico, D. R. Feldman, A. D. Jones, W. D. Collins, L. Kaatz, A low-to-no snow future and its impacts on water resources in the western United States. *Nat. Rev. Earth Environ.* **2**, 800–819 (2021).
26. A. M. Rhoades, B. J. Hatchett, M. D. Risser, W. D. Collins, N. E. Bambach, L. S. Huning, R. McCrary, E. R. Siirila-Woodburn, P. A. Ullrich, M. F. Wehner, C. M. Zarzycki, A. D. Jones, Asymmetric emergence of low-to-no snow in the midlatitudes of the American Cordillera. *Nat. Clim. Change* **12**, 1151–1159 (2022).
27. S. E. Null, L. Prudencio, Climate change effects on water allocations with season dependent water rights. *Sci. Total Environ.* **571**, 943–954 (2016).
28. D. Li, Y. Chen, L. Lyu, X. Cai, Uncovering historical reservoir operation rules and patterns: Insights from 452 large reservoirs in the contiguous United States. *Water Resour. Res.* **60**, e2023WR036686 (2024).
29. A. A. Beltran-Peña, A. Rhoades, E. Burakowski, M. Girotto, A. M. Michalak, N. S. Diffenbaugh, H. Inda-Diaz, P. D'Odorico, Future implications of enhanced

hydroclimate variability and reduced snowpack on California's water resources. *Environ. Res. Water* **1**, 025004 (2025).
30. F. Lehner, E. R. Wahl, A. W. Wood, D. B. Blatchford, D. Llewellyn, Assessing recent declines in Upper Rio Grande runoff efficiency from a paleoclimate perspective. *Geophys. Res. Lett.* **44**, 4124–4133 (2017).
31. F. Lehner, A. W. Wood, D. Llewellyn, D. B. Blatchford, A. G. Goodbody, F. Pappenberger, Mitigating the impacts of climate nonstationarity on seasonal streamflow predictability in the U.S. Southwest. *Geophys. Res. Lett.* **44**, 12,208–12,217 (2017).
32. A. M. Rhoades, P. A. Ullrich, C. M. Zarzycki, Projecting 21st century snowpack trends in western USA mountains using variable-resolution CESM. *Clim. Dym.* **50**, 261–288 (2018).
33. A. M. Marshall, J. T. Abatzoglou, S. Rahimi, D. P. Lettenmaier, A. Hall, California's 2023 snow deluge: Contextualizing an extreme snow year against future climate change. *Proc. Natl. Acad. Sci. U.S.A.* **121**, e2320600121 (2024).
34. J. Norris, S. Rahimi, L. Huang, B. Bass, C. W. Thackeray, A. Hall, Uncertainty of 21st century western U.S. snowfall loss derived from regional climate model large ensemble. *npj Clim. Atmos. Sci.* **8**, 134 (2025).
35. T. G. Shepherd, E. Boyd, R. A. Calel, S. C. Chapman, S. Dessai, I. M. Dima-West, H. J. Fowler, R. James, D. Maraun, O. Martius, C. A. Senior, A. H. Sobel, D. A. Stainforth, S. F. B. Tett, K. E. Trenberth, B. J. J. M. van den Hurk, N. W. Watkins, R. L. Wilby, D. A. Zenghelis, Storylines: An alternative approach to representing uncertainty in physical aspects of climate change. *Clim. Change* **151**, 555–571 (2018).
36. G. P. Compo, J. S. Whitaker, P. D. Sardeshmukh, Feasibility of a 100-year reanalysis using only surface pressure data. *Bull. Am. Meteorol. Soc.* **87**, 175–190 (2006).
37. L. C. Slivinski, G. P. Compo, J. S. Whitaker, P. D. Sardeshmukh, B. S. Giese, C. McColl, R. Allan, X. Yin, R. Vose, H. Titchner, J. Kennedy, L. J. Spencer, L. Ashcroft, S. Brönnimann, M. Brunet, D. Camuffo, R. Cornes, T. A. Cram, R. Crouthamel, F. Domínguez-Castro, J. E. Freeman, J. Gergis, E. Hawkins, P. D. Jones, S. Jourdain, A. Kaplan, H. Kubota, F. L. Blancq, T. C. Lee, A. Lorrey, J. Luterbacher, M. Maugeri, C. J. Mock, G. W. K. Moore, R. Przybylak, C. Pudmenzky, C. Reason, V. C. Slonosky, C. A. Smith, B. Tinz, B. Trewin, M. A. Valente, X. L. Wang, C. Wilkinson, K. Wood, P. Wyszyński, Towards a more reliable historical reanalysis: Improvements for version 3 of the twentieth century reanalysis system. *Q. J. Roy. Meteorol. Soc.* **145**, 2876–2908 (2019).
38. L. C. Slivinski, G. P. Compo, P. D. Sardeshmukh, J. S. Whitaker, C. McColl, R. J. Allan, P. Brohan, X. Yin, C. A. Smith, L. J. Spencer, R. S. Vose, M. Rohrer, R. P. Conroy, D. C. Schuster, J. J. Kennedy, L. Ashcroft, S. Brönnimann, M. Brunet, D. Camuffo, R. Cornes, T. A. Cram, F. Domínguez-Castro, J. E. Freeman, J. Gergis, E. Hawkins, P. D. Jones, H. Kubota, T. C. Lee, A. M. Lorrey, J. Luterbacher, C. J. Mock, R. K. Przybylak, C. Pudmenzky, V. C. Slonosky, B. Tinz, B. Trewin, X. L. Wang, C. Wilkinson, K. Wood, P. Wyszyński, An evaluation of the performance of the Twentieth Century Reanalysis version 3. *J. Clim.* **34**, 1417–1438 (2021).
39. E. Anderson, *A Point Energy and Mass Balance Model of a Snow Cover* (National Weather Service, 1976).
40. B. J. Hatchett, Snow level characteristics and impacts of a spring typhoon-originating atmospheric river in the Sierra Nevada, USA. *Atmosphere* **9**, 233 (2018).
41. Y. Fang, Y. Liu, D. Li, H. Sun, S. A. Margulis, Spatiotemporal snow water storage uncertainty in the midlatitude American Cordillera. *Cryosphere* **17**, 5175–5195 (2023).
42. E. R. Cook, R. Seager, M. A. Cane, D. W. Stahle, North American drought: Reconstructions, causes, and consequences. *Earth Sci. Rev.* **81**, 93–134 (2007).
43. C. Herweijer, R. Seager, E. R. Cook, J. Emile-Geay, North American droughts of the last millennium from a gridded network of tree-ring data. *J. Clim.* **20**, 1353–1376 (2007).
44. G. K. Gilbert, John Wesley Powell. *Science* **16**, 561–567 (1902).
45. J. R. Eagleman, Pan evaporation, potential and actual evapotranspiration. *J. Appl. Meteorol. Climatol.* **6**, 482–488 (1967).
46. S. Belmecheri, F. Babst, E. R. Wahl, D. W. Stahle, V. Trouet, Multi-century evaluation of Sierra Nevada snowpack. *Nat. Clim. Change* **6**, 2–3 (2016).
47. P. A. Ullrich, Z. Xu, A. M. Rhoades, M. D. Dettinger, J. F. Mount, A. D. Jones, P. Vahmani, California's drought of the future: A midcentury recreation of the exceptional conditions of 2012-2017. *Earth's Future* **6**, 1568–1587 (2018).
48. W. Reis, J. Giovando, M. Bartles, T. Dahl, A. Breverman, Snow model complexity evaluation for real-time streamflow forecasting. *J. Hydrol.* **659**, 133197 (2025).
49. A. K. Betts, R. Desjardins, D. Worth, S. Wang, J. Li, Coupling of winter climate transitions to snow and clouds over the Prairies. *J. Geophys. Res. Atmos.* **119**, 1118–1139 (2014).
50. W. Rudisill, A. Flores, J. McNamara, The impact of initial snow conditions on the numerical weather simulation of a Northern rockies atmospheric river. *J. Hydrometeorol.* **22**, 155–167 (2021).
51. K. N. Musselman, N. P. Molotch, S. A. Margulis, Snowmelt response to simulated warming across a large elevation gradient, southern Sierra Nevada, California. *Cryosphere* **11**, 2847–2866 (2017).
52. S. M. Skiles, T. H. Painter, Toward understanding direct absorption and grain size feedbacks by dust radiative forcing in snow with coupled snow physical and radiative transfer modeling. *Water Resour. Res.* **55**, 7362–7378 (2019).
53. A. L. Koshkin, B. J. Hatchett, A. W. Nolin, Wildfire impacts on western United States snowpacks. *Front. Water* **4**, 10.3389/frwa.2022.971271 (2022).
54. A. A. Harpold, P. D. Brooks, Humidity determines snowpack ablation under a warming climate. *Proc. Natl. Acad. Sci. U.S.A.* **115**, 1215–1220 (2018).
55. A. M. Marshall, T. E. Link, A. P. Robinson, J. T. Abatzoglou, Higher snowfall intensity is associated with reduced impacts of warming upon winter snow ablation. *Geophys. Res. Lett.* **47**, e2019GL086409 (2020).
56. K. Haleakala, W. T. Brandt, B. J. Hatchett, D. Li, D. P. Lettenmaier, M. Gebremichael, Watershed memory amplified the Oroville rain-on-snow flood of February 2017. *PNAS Nexus* **2**, pgac295 (2023).
57. W. T. Brandt, K. Haleakala, B. J. Hatchett, M. Pan, A review of the hydrologic response mechanisms during mountain rain-on-snow. *Front. Earth Sci.* **10**, 10.3389/feart.2022.791760 (2022).
58. E. E. Smoot, K. E. Gleason, Forest fires reduce snow-water storage and advance the timing of snowmelt across the Western U.S. *Water* **13**, 3533 (2021).
59. A. F. Nolin, M. P. Girardin, J. C. Tardif, X. J. Guo, F. Conciatori, Y. Bergeron, A 247-year tree-ring reconstruction of spring temperature and relation to spring flooding in eastern boreal Canada. *Int. J. Climatol.* **42**, 6479–6498 (2022).
60. I. Gillespie, L. Haimberger, G. P. Compo, P. W. Thorne, Assessing homogeneity of land surface air temperature observations using sparse-input reanalyses. *Int. J. Climatol.* **43**, 736–760 (2023).
61. J. T. Abatzoglou, K. T. Redmond, Asymmetry between trends in spring and autumn temperature and circulation regimes over western North America. *Geophys. Res. Lett.* **34**, L18808 (2007).
62. P. M. Forster, C. Smith, T. Walsh, W. F. Lamb, R. Lamboll, B. Hall, M. Hauser, A. Ribes, D. Rosen, N. P. Gillett, M. D. Palmer, J. Rogelj, K. von Schuckmann, B. Trewin, M. Allen, R. Andrew, R. A. Betts, A. Borger, T. Boyer, J. A. Broersma, C. Buontempo, S. Burgess, C. Cagnazzo, L. Cheng, P. Friedlingstein, A. Gettelman, J. Gütschow, M. Ishii, S. Jenkins, X. Lan, C. Morice, J. Mühle, C. Kadow, J. Kennedy, R. E. Killick, P. B. Krummel, J. C. Minx, G. Myhre, V. Naik, G. P. Peters, A. Pirani, J. Pongratz, C. F. Schleussner, S. I. Seneviratne, S. Szopa, P. Thorne, M. V. M. Kovilakam, E. Majamäki, J. P. Jalkanen, M. van Marle, R. M. Hoesly, R. Rohde, D. Schumacher, G. van der Werf, R. Vose, K. Zickfeld, X. Zhang, V. Masson-Delmotte, P. Zhai, Indicators of Global Climate Change 2023: Annual update of key indicators of the state of the climate system and human influence. *Earth Syst. Sci. Data* **16**, 2625–2658 (2024).
63. L. Mudryk, C. Mortimer, C. Derksen, A. Elias Chereque, P. Kushner, Benchmarking of snow water equivalent (SWE) products based on outcomes of the SnowPEx+ Intercomparison Project. *Cryosphere* **19**, 201–218 (2025).
64. E. Anderson, "Snow accumulation and ablation model - SNOW-17," January 2006; www.weather.gov/media/owp/oh/hrl/docs/22snow17.pdf.
65. A. L. Lang, K. Pegion, E. A. Barnes, Introduction to special collection: "Bridging weather and climate: Subseasonal-to-seasonal (S2S) prediction". *J. Geophys. Res. Atmos.* **125**, e2019JD031833 (2020).
66. S. Wu, M. Luo, R. Zhao, J. Li, P. Sun, Z. Liu, X. Wang, P. Wang, H. Zhang, Local mechanisms for global daytime, nighttime, and compound heatwaves. *NPJ Clim. Atmos. Sci.* **6**, 36 (2023).
67. K. Guirguis, A. Gershunov, B. J. Hatchett, M. J. De Florio, A. C. Subramanian, R. Clemesha, L. D. Monache, F. M. Ralph, Subseasonal prediction of impactful California winter weather in a hybrid dynamical-statistical framework. *Geophys. Res. Lett.* **50**, e2023GL105360 (2023).
68. A. K. Srivastava, R. Grotjahn, A. M. Rhoades, P. A. Ullrich, Large-scale statistically meaningful patterns (LSMPs) associated with precipitation extremes over Northern California. *J. Geophys. Res. Atmos.* **130**, e2024JD041307 (2025).
69. C. M. Patricola, J. P. O'Brien, M. D. Risser, A. M. Rhoades, T. A. O'Brien, P. A. Ullrich, D. A. Stone, W. D. Collins, Maximizing ENSO as a source of western US hydroclimate predictability. *Clim. Dyn.* **54**, 351–372 (2020).
70. H. Huang, C. M. Patricola, E. Bercos-Hickey, Y. Zhou, A. Rhoades, M. D. Risser, W. D. Collins, Sources of subseasonal-to-seasonal predictability of atmospheric rivers and precipitation in the western United States. *J. Geophys. Res. Atmos.* **126**, e2020JD034053 (2021).
71. C. Körner, W. Jetz, J. Paulsen, D. Payne, K. Rudmann-Maurer, E. M. Spehn, A global inventory of mountains for bio-geographical applications. *Alp. Botany* **127**, 1–15 (2017).
72. M. Sturm, G. E. Liston, Revisiting the global seasonal snow classification: An updated dataset for earth system applications. *J. Hydrometeorol.* **22**, 2917–2938 (2021).
73. W. W. Immerzeel, A. F. Lutz, M. Andrade, A. Bahl, H. Biemans, T. Bolch, S. Hyde, S. Brumby, B. J. Davies, A. C. Elmore, A. Emmer, M. Feng, A. Fernández, U. Haritashya, J. S. Kargel, M. Koppes, P. D. A. Kraaijenbrink, A. V. Kulkarni, P. A. Mayewski, S. Nepal, P. Pacheco, T. H. Painter, F. Pellicciotti, H. Rajaram, S. Rupper, A. Sinisalo, A. B. Shrestha, D. Viviroli, Y. Wada, C. Xiao, T. Yao, J. E. M. Baillie, Importance and vulnerability of the world's water towers. *Nature* **577**, 364–369 (2020).
74. M. S. Pelto, M. Dryak, J. Pelto, T. Matthews, L. B. Perry, Contribution of glacier runoff during heat waves in the nooksack river basin USA. *Water* **14**, 1145 (2022).
75. A. Cremona, M. Huss, J. M. Landmann, J. Borner, D. Farinotti, European heat waves 2022: Contribution to extreme glacier melt in Switzerland inferred from automated ablation readings. *Cryosphere* **17**, 1895–1912 (2023).

76. A. Ayala, D. Farías-Barahona, M. Huss, F. Pellicciotti, J. McPhee, D. Farinotti, Glacier runoff variations since 1955 in the Maipo River basin, in the semiarid Andes of central Chile. *Cryosphere* **14**, 2005–2027 (2020).
77. Á. González-Reyes, M. Jacques-Coper, C. Bravo, M. Rojas, R. Garreaud, Evolution of heatwaves in Chile since 1980. *Weather Clim. Extrem.* **41**, 100588 (2023).
78. Z. Hausfather, An assessment of current policy scenarios over the 21st century and the reduced plausibility of high-emissions pathways. *Dialogues Clim. Change* **2**, 26–32 (2025).
79. N. E. Bambach, A. M. Rhoades, B. J. Hatchett, A. D. Jones, P. A. Ullrich, C. M. Zarzycki, Projecting climate change in South America using variable-resolution community Earth system model: An application to Chile. *Int. J. Climatol.* **42**, 2514–2542 (2022).
80. A. Heggli, B. Hatchett, A. Schwartz, T. Bardsley, E. Hand, Toward snowpack runoff decision support. *iScience* **25**, 104240 (2022).
81. M. Allen, et al., Special report: Global warming of 1.5 C. *Intergovernmental Panel on Climate Change* (*IPCC*) **677**, 393 (2018).
82. U. Schulzweida, CDO user guide, Zenodo (2023); https://doi.org/10.5281/zenodo.10020800.
83. P. A. Ullrich, C. M. Zarzycki, E. E. McClenny, M. C. Pinheiro, A. M. Stansfield, K. A. Reed, TempestExtremes v2.1: A community framework for feature detection, tracking, and analysis in large datasets. *Geosci. Model Dev.* **14**, 5023–5048 (2021).
84. M. He, T. S. Hogue, K. J. Franz, S. A. Margulis, J. A. Vrugt, Characterizing parameter sensitivity and uncertainty for a snow model across hydroclimatic regimes. *Adv. Water Resour.* **34**, 114–127 (2011).
85. A. Ohmura, Physical basis for the temperature-based melt-index method. *J. Appl. Meteorol.* **40**, 753–761 (2001).
86. National Weather Service, "IV.2.2-SNOW-17: Initial parameter values for the Hydro-17 Snow model," in *OHD/HL - NWSRFC Users Manual* (National Weather Service, National Oceanic and Atmospheric Administration, 1–12, 2004).
87. T. Chen, W. B. Rossow, Y. Zhang, Radiative effects of cloud-type variations. *J. Clim.* **13**, 264–286 (2000).
88. B. N. Abrahim, N. J. Cullen, J. P. Conway, A decade of surface meteorology and radiation fluxes at Brewster Glacier in the Southern Alps of New Zealand. *Int. J. Climatol.* **42**, 1612–1631 (2022).
89. W. Rudisill, D. Feldman, C. J. Cox, L. Riihimaki, J. Sedlar, Seasonality and albedo dependence of cloud radiative forcing in the upper colorado river basin. *J. Geophys. Res. Atmos.* **130**, e2024JD042366 (2025).
90. D. R. DeWalle, A. Rango, "Chapter 6 - Snowpack energy exchange: Basic theory," in *Principles of Snow Hydrology* (Cambridge Univ. Press, 2008), pp. 146–181.
91. K. S. Jennings, T. G. F. Kittel, N. P. Molotch, Observations and simulations of the seasonal evolution of snowpack cold content and its relation to snowmelt and the snowpack energy budget. *Cryosphere* **12**, 1595–1614 (2018).
92. H. Hersbach, B. Bell, P. Berrisford, S. Hirahara, A. Horányi, J. Muñoz-Sabater, J. Nicolas, C. Peubey, R. Radu, D. Schepers, A. Simmons, C. Soci, S. Abdalla, X. Abellan, G. Balsamo, P. Bechtold, G. Biavati, J. Bidlot, M. Bonavita, G. de Chiara, P. Dahlgren, D. Dee, M. Diamantakis, R. Dragani, J. Flemming, R. Forbes, M. Fuentes, A. Geer, L. Haimberger, S. Healy, R. J. Hogan, E. Hólm, M. Janisková, S. Keeley, P. Laloyaux, P. Lopez, C. Lupu, G. Radnoti, P. de Rosnay, I. Rozum, F. Vamborg, S. Villaume, J. N. Thépaut, The ERA5 global reanalysis. *Q. J. Roy. Meteorol. Soc.* **146**, 1999–2049 (2020).
93. B. J. Hatchett, Seasonal and ephemeral snowpacks of the conterminous United States. *Hydrology* **8**, 32 (2021).
94. D. S. Wilks, *Statistical Methods in the Atmospheric Sciences* (Academic Press, 2011), vol. 100.
95. N. C. Cristea, I. Breckheimer, M. S. Raleigh, J. HilleRisLambers, J. D. Lundquist, An evaluation of terrain-based downscaling of fractional snow covered area data sets based on LiDAR-derived snow data and orthoimagery. *Water Resour. Res.* **53**, 6802–6820 (2017).
96. Stan Development Team, Stan Modeling Language Users Guide and Reference Manual, version 2.36.0, Stan (2024); https://mc-stan.org.
97. A. Vehtari, A. Gelman, D. Simpson, B. Carpenter, P. C. Burkner, Rank-normalization, folding, and localization: An improved $\widehat{R}$ for assessing convergence of MCMC (with Discussion). *Bayesian Anal.* **16**, 667–718 (2021).
98. S. Duan, P. Ullrich, M. Risser, A. Rhoades, Using temporal deep learning models to estimate daily snow water equivalent over the rocky mountains. *Water Resour. Res.* **60**, e2023WR035009 (2024).
99. J. I. López-Moreno, J. Revuelto, M. Gilaberte, E. Morán-Tejeda, M. Pons, E. Jover, P. Esteban, C. García, J. W. Pomeroy, The effect of slope aspect on the response of snowpack to climate warming in the Pyrenees. *Theor. Appl. Climatol.* **117**, 207–219 (2014).
100. A. Mahesh, W. Collins, B. Bonev, N. Brenowitz, Y. Cohen, J. Elms, P. Harrington, K. Kashinath, T. Kurth, J. North, T. OBrien, M. Pritchard, D. Pruitt, M. Risser, S. Subramanian, J. Willard, Huge ensembles part I: Design of ensemble weather forecasts using spherical fourier neural operators. arXiv:2408.03100 [physics.ao-ph] (2025).
101. H. Hersbach, Decomposition of the continuous ranked probability score for ensemble prediction systems. *Weather Forecast.* **15**, 559–570 (2000).
102. S. Allen, J. Bhend, O. Martius, J. Ziegel, Weighted verification tools to evaluate univariate and multivariate probabilistic forecasts for high-impact weather events. *Weather Forecast.* **38**, 499–516 (2023).
103. S. A. Baker, A. W. Wood, B. Rajagopalan, J. Prairie, C. Jerla, E. Zagona, R. A. Butler, R. Smith, The colorado river basin operational prediction testbed: A framework for evaluating streamflow forecasts and reservoir operations. *J Am. Water Resour. Assoc.* **58**, 690–708 (2022).
104. K. N. Musselman, M. P. Clark, C. Liu, K. Ikeda, R. Rasmussen, Slower snowmelt in a warmer world. *Nat. Clim. Change* **7**, 214–219 (2017).
105. D. Marks, J. Dozier, Climate and energy exchange at the snow surface in the Alpine Region of the Sierra Nevada: 2. Snow cover energy balance. *Water Resour. Res.* **28**, 3043–3054 (1992).
106. D. W. Cline, Snow surface energy exchanges and snowmelt at a continental, midlatitude Alpine site. *Water Resour. Res.* **33**, 689–701 (1997).
107. Copernicus Climate Change Service Climate Data Store, "Copernicus Climate Change Service (C3S): ERA5: Fifth generation of ECMWF atmospheric reanalyses of the global climate," 2017; https://cds.climate.copernicus.eu/cdsapp#!/dataset/reanalysis-era5-pressure-levels?tab=overview.

Acknowledgments

Funding: This study was primarily funded by the Director, Office of Science, Office of Biological and Environmental Research of the US Department of Energy Regional and Global Model Analysis (RGMA) and MultiSector Dynamics (MSD) Program Areas. A.M.R., J.S.N., M.R., A.M., A.S., M.W., and Y.Z. were funded by the "Calibrated and systematic characterization, attribution and detection of extremes (CASCADE)" Science Focus Area (award no. DE-AC02-05CH11231). A.M.R., R.C., S.R., C.R., A.S., and A.D.J. were funded by the "An integrated evaluation of the simulated hydroclimate system of the continental US" (HyperFACETS) project (award no. DE-SC0016605). A.M.R., L.S.H., and D.M. were funded by the NOAA Climate Program Office (CPO) Modeling, Analysis, Predictions, and Projections (MAPP) and National Integrated Drought Information System (NIDIS) programs on the "Understanding heat wave–snow drought relationships across the western United States" project (award no. NOAA-OAR-CPO-2023-2007440), and S.R. was funded by the NOAA MAPP-NIDIS project "Towards predicting drought and subsequent water resource challenges at landscape-resolving scales across the western U.S." (award no. NA23OAR4310633-T1-01). W.R. was supported by the US Department of Energy, Office of Science, Office of Biological and Environmental Research, and the Atmospheric System Research Program project "Surface Atmosphere Integrated Field Laboratory (SAIL)" under US Department of Energy contract no. DE-AC02-05CH11231. A.B.-P. was funded by the Stanford Doerr School of Sustainability Dean's Postdoctoral Fellowship from Stanford University. S.H. was funded by the Agriculture and Food Research Initiative Competitive Grant (award no. 2021-69012-35916) from the USDA National Institute of Food and Agriculture. **Author contributions:** Conceptualization: A.M.R., J.S.N., W.R., B.J.H., M.R., M.L., A.M.M., R.M., and A.D.J. Methodology: A.M.R., J.S.N., W.R., B.J.H., M.R., and A.D.J. Investigation: A.M.R., J.S.N., W.R., B.J.H., A.J., A.M., and D.M. Formal analysis: A.M.R., J.S.N., W.R., and A.J. Visualization: A.M.R., J.S.N., W.R., B.J.H., M.R., A.J., M.L., D.M., and A.D.J. Data curation: A.M.R., J.S.N., W.R., A.J., and M.R. Validation: A.M.R., J.S.N., W.R., and A.J. Resources: A.M.R., J.S.N., M.R., A.J., and A.D.J. Funding acquisition: A.M.R., J.S.N., M.R., D.M., and A.D.J. Software: A.M.R., J.S.N., W.R., A.J., and M.R. Supervision: A.M.R., B.J.H., and A.D.J. Project administration: A.M.R. and A.D.J. Writing—original draft: A.M.R., J.S.N., W.R., B.J.H., M.R., A.B.-P., A.H., S.H., L.S.H., M.L., A.M., S.R., C.R., A.S., M.W., and Y.Z. Writing—review and editing: A.M.R., J.S.N., W.R., B.J.H., A.B.-P., A.H., S.H., L.S.H., M.L., A.M., A.M.M., R.M., D.M., S.R., M.S.R., C.R., A.S., M.W., Y.Z., and A.D.J. **Competing interests:** The authors declare that they have no competing interests. **Data, code, and materials availability:** This study did not generate new materials. All data and code needed to evaluate or reproduce the results in this study are present in the paper, the Supplementary Materials, or in the following repository. The 20CRv3 postprocessed data and snow-eater heat-wave tracking, analysis, and plotting code can be found via a publicly accessible repository (Science Gateway) through the National Energy Research Scientific Computing Center. https://portal.nersc.gov/archive/home/a/arhoades/www/NOAA_Snow_Drought_Heatwave.

Submitted 9 August 2025
Accepted 11 June 2026
Published 5 August 2026
10.1126/sciadv.aeb3361

Snow-eater heat waves of the western United States

Alan M. Rhoades, Joshua Snowball North, William Rudisill, Benjamin J. Hatchett, Mark Risser, Areidy Beltran-Peña, Anne Heggli, Scott Hotaling, Laurie S. Huning, Andrew Joros, Matthew LaPlante, Ankur Mahesh, Adrienne M. Marshall, Rachel McCrary, Daniel McEvoy, Stefan Rahimi, Mark S. Raleigh, Calen Randall, Abhishekh Srivastava, Michael Wehner, Yang Zhou, and Andrew D. Jones

Sci. Adv. **12** (32), eaeb3361. DOI: 10.1126/sciadv.aeb3361

Science Advances (ISSN 2375-2548) is published by the American Association for the Advancement of Science. 1200 New York Avenue NW, Washington, DC 20005. The title *Science Advances* is a registered trademark of AAAS.